Catalyst Structure-based Hydroxymethylfurfural (HMF) Hydrogenation Mechanisms, Activity and Selectivity over Ni

Brett Pomeroy[a], Miha Grilc[a], Sašo Gyergyek[b], Blaž Likozar[a,*]

[a] *Department of Catalysis and Chemical Reaction Engineering, National Institute of Chemistry, Hajdrihova 19, 1000 Ljubljana, Slovenia*

[b] *Department of Synthesis of Materials, Jožef Stefan Institute, Jamova Cesta 39, 1000 Ljubljana, Slovenia*

ARTICLE INFO

---

*Corresponding author. Tel.: +386 1 4760 281; fax: +386 1 4760300.

E-mail address: blaz.likozar@ki.si (B. Likozar).

ABSTRACT

Catalytic hydrodeoxygenation of hydroxymethylfurfural was investigated in a three-phase batch reactor over a range of reaction temperatures (170–230 °C), under 5 MPa of hydrogen, and tetrahydrofuran solvent. Nickel-based carbon-supported catalysts were also promoted by lanthanum and niobium, despite promoters alone demonstrated no activity. Based on experimentally-obtained liquid products, a reaction pathway was proposed and a microkinetic model was established, by considering adsorption, desorption and surface reaction kinetics, mass transfer and thermodynamics. An unpromoted Ni/C resulted in primarily unsaturated furan diol, a highly desirable intermediate in the polymer industry. As reaction temperatures increased >200 °C, dehydration yielded deoxygenated products suitable for solvents and biofuel. In spite of enhancements to reducibility, La-promotion significantly decreased both hydrogenation (8-times) and deoxygenation (25-times) rate constants. Alternatively, Nb-incorporation offered additional acidity, while lower activation energies resulted in 200% higher deoxygenation rates via dehydration reactions and humin formation at lower temperatures. It exhibited the highest deoxygenation activity.

Keywords:

Hydroxymethylfurfural

Catalytic hydrodeoxygenation

Hydrogenation and dehydroxylation

Bio-based chemicals

Reaction kinetics

1. Introduction

Considering the worldwide challenges regarding climate change, pollution, and the ever growing global energy consumption as a result from the current use of non-renewable fossil fuels, more sustainable alternatives are required that shift us towards more renewable feedstocks that are environmentally friendly and carbon neutral. Presently, reports indicate that renewables comprise only around 5% of the total world energy consumption, falling considerably behind the combined contribution of oil, coal, and natural gas of 85%.

Lignocellulosic biomass has progressively been considered a promising renewable substitute for the production of bio-based fuels and chemicals with tremendous potential due to its abundancy, relatively low cost, and does not compete with food resources [1]. Lignocellulosic biomass is composed of 3 main components; cellulose, hemicellulose, and lignin. Since cellulose, a polysaccharide of C_6 hexose sugars, comprises approximately half of all lignocellulosic biomass, its conversion to valuable chemicals and fuels has been of vital significance [2].

Specifically, the formation of 5-hydroxymethylfurfural (HMF) from glucose has received particular attention for its immense versatility in forming a vast range of platform chemicals for bio-polymer and biofuel production, even being referred to as a *sleeping giant* in the field of renewables [3,4,5]. HMF contains three desirable functional constituents (an alcohol, a carbonyl group in the form of an aldehyde, and furan ring) which permits flexible access to several industrially relevant compounds. Of particular interest are dimethylfuran (DMF), and the diols 2,5-bishydroxymethalfuran (BHMF), and 2,5-bishydroxymethyltetrahydrofuran (BHMTF). DMF has been recognized as a biofuel more suitable than bioethanol with a higher energy density, high research octane number, and lower water solubility allowing it to be more easily blended into gasoline [6–8]. BHMF and BHMTF are highly desirable for applications in the polymer industry in the manufacturing of

polyesters and heat insulating polymers, which are currently made exclusively from petroleum-based feedstocks [9,10].

Catalytic hydrotreatment with hydrodeoxygenation (HDO) has been accepted as one of the most promising conversion routes to obtain these value-added chemicals as it takes advantage of the decades of extensive research that has been employed in conventional petroleum hydrotreating involving hydrodesulfurization which it is closely linked [11]. Generally, HDO occurs at moderate temperatures (100 - 250 °C) and high hydrogen pressures (3 - 10 MPa) in the presence of a heterogeneous catalyst where oxygen is typically expelled in the form of H_2O [12]. Nickel has been identified as an ideal transition metal that elicits adequate hydrogenation activity [13–15]. Additionally, its low cost and availability makes it highly attractive in comparison to noble metals such as Pt, Pd, Rh, and Ru, although hydrogenation activity and stability are typically substandard in comparison [16]. To increase activity and stability of transition metal catalysts, additional metals (promoters) are added to the catalyst to contribute additional functionality and enhance performance. The addition of a second, promoter metal to nickel catalysts has been widely demonstrated to greatly enhance catalytic activity and augment product selectivity. This study investigates the impact of lanthanum and niobium on the hydrogenation activity of nickel-based catalysts for HDO of HMF. Both lanthanum and niobium have demonstrated great potential as effective Ni promoters for hydrogenation reactions by improving particle dispersion and reducibility, though by opposing behaviors [16-19]. Lanthanum has been commonly employed as a nickel promoter, which has been described to increase reducibility by forming a layer around the support (‘under’ nickel) that weakens metal-support interactions, thus enhancing metallic dispersion and thermal stability [19–22]. Niobium incorporated into nickel-containing catalysts has been shown to also enhance metal dispersion, instead by partially encompassing NiO particles (‘over’ nickel), preventing particle growth and agglomeration which can occur

during high temperature pretreatments [23–25]. Activated carbon was selected as support material as it provides a high surface area for maximum metal dispersion, and its relative inert surface evades high rates of undesirable side reactions compared to other supports such as alumina and silica [26] [27].

The same intrinsic flexible nature of HMF also creates major challenges when attempting to control the selectivity of catalytic reactions and often results in a complex mixture of products [28]. Alongside hydrodeoxygenation, several alternative side reactions can also arise such as decarbonylation, (hydro)cracking, and saturation of the furan ring depending on the reaction conditions and catalyst used, causing difficulties in accurately determining reaction mechanisms [29]. Several publications have been able to achieve high product selectivities of both DMF and BHMF. Kong et al. achieved 92% selectivity of DMF with comparable alumina-supported nickel catalysts in 1,4-dioxane as the solvent [14]. Yu et al. obtained 96% selectivity to BHMF when using Ni-Fe nanoparticles supported on carbon nanotubes in n-butanol [30]. Likewise, comparable studies for the selective catalytic hydrotreatment of furfural, an analogous furanic derived from pentoses, have also been reported with excellent selectivies [31][32]. Although high selectivies have been reached, a comprehensive understanding of their reaction kinetics is essentially absent. Kinetic modelling can provide valuable insights for the in-depth understanding and describing of surface chemistry on a fundamental level, and subsequent improvements in the design of catalytic systems which is not possible through conventional methods. These microkinetic models, based on first-principles, consider several elementary steps within the experimental system including; gas solubility in the liquid phase, adsorption and desorption kinetics, and catalyst surface reactions. Kinetic studies on HMF are scarce in the literature and have primarily been restricted to the formation of HMF from sugars rather than its catalytic conversion to value-added products [33–35]. The rare kinetic study that does involve HMF

conversion have been based on simple systems that provide limited knowledge [36,37]. Kinetic studies are of high importance and its further development is essential to better understand optimal operating conditions and catalyst compositions to reach maximum yields of a desired product.

In this study, the microkinetics of HMF HDO in a batch system is reported at relevant temperatures (170−230 °C) for hydrogenation, and concentrations of all liquid intermediates and products as a function of time are included in the kinetic analysis. Based on experimental data and detectable compounds, a reaction pathway is proposed and a kinetic scheme was employed to model experimental conclusions. To our knowledge, a detailed microkinetic model of HDO of HMF is generally lacking in the literature, therefore this study aims to cultivate a microkinetic model with the capability to predict reaction rates with experimental data using promoted activated carbon-supported nickel-based catalysts. These promoters were selected as they have been shown to beneficially influence nickel metallic species and reducibility, and their irreducible nature (at least under the implemented experimental conditions in the case of niobium) is anticipated to not provide any additional metallic active phase themselves [38–40].

2. Experimental

2.1 Materials

All gases, chemical reactants, and calibration standards were purchased from various commercial suppliers and used as is without further purification; (5-Hydroxymethylfurfural (>97 wt.%, Carbonsynth, reference number FH10853), 5-methylfurfural (99 wt.%, Sigma Aldrich), dimethylfuran (99 wt.%, Sigma Aldrich), 2,5-bis(hydroxymethyl)furan (98 wt.%, VWR), 2,5-bis(hydroxymethyl)tetrahydrofuran (>95 wt.%, Carbosynth), (5-methyl-2-

furyl)methanol (98 wt.%, Carbosynth), hydrogen (5.0, Messer, Bad Soden am Taunas, Germany), nitrogen (5.0, Messer, Bad Soden am Taunas, Germany), NH_3 (5 vol% in He, Linde, Pullach, Germany), helium (5.0 Messer, Bad Soden am Taunas, Germany), carbon monoxide (5 vol% CO in He, Linde, Pullach, Germany), and tetrahydrofuran (>95 wt.%, EMD Millipore) used as solvent. Lanthanum (III) nitrate hexahydrate (99 wt.%, Honeywell Fluka) and nickel (II) nitrate hexahydrate (97 wt.%, Sigma-Aldrich, St. Louis, MO, USA, reference number 72253), niobium pentachloride (99 wt.%, Sigma-Aldrich, St. Louis, MO, USA) were implemented in catalyst preparation using Vulcan XC-72R carbon powder (Cabot Corporations, Bilerica, MA, USA) as support. VXC-72R carbon powder has a bulk density between 20-380 kg/m^3 and a density of 1.7-1.9 g/cm^3.

2.2 Catalyst preparation

Catalysts containing nickel and/or lanthanum were prepared by incipient wetness impregnation using aqueous solutions of $Ni(NO_3)_2{\cdot}6H_2O$ and $La(NO_3)_3{\cdot}6H_2O$ precursors dissolved in deionized water that was equal to the total pore volume of the activated carbon to obtain 5 wt.% and 10 wt.%, respectively (5Ni10La). Prior to impregnation, the activated carbon (VXC-72R) was crushed and sieved to obtain the $40 - 100$ µm fraction to ease any internal mass-transfer limitations within the catalysts particle. Following impregnation, catalysts were dried at 110 °C overnight in an oven. NiLa catalyst was impregnated in 2 subsequent steps; firstly lanthanum was impregnated, dried, followed by nickel impregnation and drying. Niobium-doped catalysts were prepared by ammonium precipitation where activated carbon was vigorously mixed under reflux at 85 °C in absolute ethanol, ammonium solution, and specific amount of pentachloride to obtain the desired 10 wt.% loading. After filtration and cleaning with deionized water, the catalysts were dried overnight at 110 °C and

subsequently impregnated with nickel nitrate exactly as mentioned above. Incipient wetness impregnation was chosen for lanthanum promotion as this has been reported to be ideal in forming a thorough layer on the catalyst surface, as opposed to ammonium precipitation used for niobium promotion which is more suitable to form fine and uniform particles [41] [42]. These preparation methods were expected to best achieve the 'under' 'over' benefits to nickel dispersion and reducibility previously mentioned.

2.3 Catalyst Characterization

2.3.1 Surface and Textural Properties

Surface and textural properties of the blank support and doped-activated carbon catalysts were analyzed with nitrogen physisorption; specifically, adsorption-desorption isotherms to determine specific surface area (S_{BET}), average pore diameter (d_p), and pore volume (V_P) using an ASAP 2020 gas adsorption instrument (Micrometrics, Norcross, GA, USA). Catalyst composition was measured by inductively coupled plasma - mass spectrometry (ICP-MS) to determine actual metal loadings in addition to final reaction mixtures to identify if any metal leaching was present. Morphological properties of catalysts particles were characterized by field-emission scanning electron microscopy (FE-SEM) (SUPRA 35 VP, Carl Zeiss, Jena, Germany). Transmission Electron Microscopy analysis was conducted at 200 kV using a thermionic electron-source TEM JEOL model 2100. Particle size distribution is presented as equivalent diameters for at least 100 individual particles, such that the diameter of a circle having equal surface area as the imaged particle. The empirical number-weighted distribution functions were fitted with a normal distribution function. The average size (d_{NTEM}) with standard deviation (σ_{NTEM}) are the arithmetic moments normal distribution function. X-ray diffraction (XRD) patterns were characterized using PW3040/60

X'Pert PRO MPD diffractometer at 35 kV and 45 mA with Cu Kα radiation source (λ = 0.154056 nm) in the 2θ range from 10° to 80°, and using JCPDS database for reference. The X-ray photoelectron spectroscopy (XPS) analysis were performed on a PHI-TFA XPS spectrometer manufactured by Physical Electronics Inc. coupled with a Mg X-ray source. The analyzed area was 0.4 mm in diameter. The high-energy resolution spectra were acquired with energy analyzer operating at resolution of 0.6 eV and pass energy of 29 eV. The accuracy of binding energies was about ±0.3 eV. Catalysts were reduced under hydrogen atmosphere with the same conditions as applied prior to activity tests.

2.3.2 Hydrogen-temperature programmed reduction

Hydrogen temperature-programmed reduction (H_2-TPR) was performed with a Micrometrics AutoChem II Chemisorption Analyser (Micrometrics, Norcross, GA, USA). Initially, 100 mg of catalyst was introduced into a quartz U-tube and pretreated under 50 mL min^{-1} of argon at 300 °C for 30 minutes with a heating rate of 30 K min^{-1} before reduction. Immediately following, the sample was subjected with 40 mL min^{-1} of a 5 vol% H_2 in Ar mixture at a constant heating rate of 10 K min^{-1} up to a maximum of 900 °C. Hydrogen consumption was determined using a TCD detector and a calibration using CuO.

2.3.3 Ammonia / carbon monoxide-temperature programmed desorption

Ammonia and carbon monoxide temperature programmed desorption (NH_3−TPD / CO−TPD) analysis were performed with a Micrometrics AutoChem II Chemisorption Analyser (Micrometrics, Norcross, GA, USA). Prior to TPD, 100 mg catalyst samples were initially pretreated under the same reduction conditions used for experiments (400 °C for 3 hours). Samples were subjected to 40 mL min^{-1} of ammonia or carbon monoxide mixtures (10 vol% NH_3 or 5 vol% CO in He) at 60 °C before being purged with He and heated-up to

600 °C with a constant heating rate of 10 K min^{-1}. Desorbed compounds were detected using a TCD detector and preferred mass spectrums were identified with a GSD 301 T3 Thermostar Mass Spectrometer. Metallic and acid sites were calculated based on known response of calibration gas mixtures. Diffuse reflectance infrared Fourier transform (DRIFT) experiments were attempted with a DiffusIR cell (PIKE Technologies) attached to Perkin Elmer Frontier spectrometer using pyridine as the probe molecule. 10 mg samples of catalyst was initially pre-treated for 20 minutes in a 100 mL min^{-1} flow of N_2 at 350 °C, left to cool for 25 minutes, than saturated with pyridine vapour in a 50 mL min^{-1} flow of N_2 gas stream for 10 minutes and subsequently evacuated for 10 minutes at 10^{-5} mbar (Pfeiffer Vacuum turbomolecular pump, model HiCube). The spectra collected are the average of 32 scans with a resolution of 4 cm^{-1} and over 1000–4000 cm^{-1} wave number range.

2.4 Catalytic activity tests

Catalytic hydrodeoxygenation reactions were conducted in 75 mL multi-reactor stainless steel batch reactor system (Parr 5000 Series). Activity tests were performed with 0.1 g of catalyst (weight of pre-reduced catalyst), 40 mL of THF, and 1 g of HMF. Prior to catalytic tests, catalysts were reduced at 400 °C for 3 hours with a heating rate of 10 K min^{-1} and a pure hydrogen flow of 40 mL min^{-1}. Reactor temperatures ranging from 170 – 230 °C with a heating rate of 5 K min^{-1} were implemented and reactions lasted 6 hours once the desired reaction temperature was reached. Mixing was induced by magnetic stir bars with a maximum stirring speed of 1200 min^{-1} to ensure negligible external mass transfer effect between gas-liquid-solid phases. Following purging three times with nitrogen and hydrogen to ensure no residual air was left in the system, the reactor was pressurized with 5.0 MPa of H_2 to ensure the amount of hydrogen was well in excess with an approximate H_2:O ratio of 20:1. Liquid samples were collected once the desired reaction temperature was achieved and

then at every hour following during isothermal conditions from the same experiment. Immediately following activity tests, the reactors were quenched in water until a final temperature of 40 °C was reached and final liquid mixtures were collected.

After the initial activity test, the spent catalysts were subjected to recyclability tests. Following the first reaction, catalysts were separated from the liquid phase by centrifugation, washed with THF twice, dried in nitrogen, and then pretreated in hydrogen under the same conditions as prior (400 °C for 3 hours, 40 mL min^{-1}) before the next activity tests. After three recycled tests (R1-R3), the catalysts were washed once again in THF, then calcined in air at 400 °C for 2 hours just before the final reduction pretreatment in the attempt to regenerate the recycled catalyst (R4).

2.5 Product Analysis

Liquid samples were filtered with 45 µm PET filters and then quantitatively evaluated off-line by gas chromatography with flame ionization detector (GC-FID) (2010 Ultra, Shimadzu, Kyoto, Japan). Compounds were separated by Zebron ZB-5MS capillary column (60 m × 0.25 mm × 0.25 µm, Phenomenex, Torrance, CA, USA) and identified with a mass spectrometer. GC analysis parameters were set with a starting oven temperature of 60 °C and subsequent heat-up to match the injector temperature of 290 °C. Calibration was determined for each product with commercially purchased external standards.

The catalytic activity test with 5Ni catalyst at 230 °C was performed in triplicate to validate the reproducibility of catalytic activity tests. Mean concentrations of the triplicates are shown in Figure S.1 and standard deviations of the mean are shown as error bars. The average standard deviation of the mean for all products was 0.003.

Further analysis of the gas phase, spent catalyst, and humin formation in liquid phase was conducted to investigate where the loss in carbon balance occurred. Gas products were

analyzed offline with a Micro-GC (490 Micro GC System, Agilent Technologies, Santa Clara, CA, USA) by the separation on PoraPLOT U (PPU) and MolSieve 5A (MS5A) columns and quantification by TCD detector. The gas phase from all tests detected negligible CO or CO_2 production (<1%). Thermal gravimetric analysis (TGA) was conducted to evaluate the coking of the catalyst using RuboTherm TG with dynamic GDS on ~10 mg sample of spent catalysts in both air and nitrogen environments up to 700 °C. Finally, size-exclusion chromatography (SEC) was performed (Thermo Scientific Ultimate 3000, ThermoFischer, Waltham, MA, USA) with UV detector and polystyrene standards, following a similar procedure reported elsewhere [43], to follow the eventual formation of oligomers.

3. Results and Discussion

3.1 Catalyst Characterization

3.1.1 Surface and Textural Properties

N_2 physisorption results are reported in Table 1. N_2 adsorption-desorption isotherms are shown in Figure S.7, in which the blank carbon support and all promoted catalysts displayed similar isotherm characteristics. Due to the fact that VXC-72R activated carbon contains large quantities of micropores (<2 nm), calculated surface areas, average pore size and pore volumes of catalysts should be considered apprehensively. Nevertheless, it would appear that the initial impregnation of lanthanum blocks a large portion of pores as surface area (S_{BET} and t-plot areas) and pore volume are significantly lower in comparison to the bare AC support and 5Ni catalyst. Nickel catalysts doped with niobium were observed to have almost identical surface area and pore volume. These variations in textural properties between catalysts is to be expected as a result from the different catalyst preparation methods conducted. As mentioned previously, incipient wetness impregnation of lanthanum was

implemented to form a thorough layer on the catalyst surface, thus leading to the loss in specific surface area, increase in the average pore diameter, and decrease in pore volume via blocking of smaller pores. Alternatively, the minimal difference in specific surface area, pore volume and average pore diameter observed between the Ni and NiNb catalysts is due to the more fine niobium particles that have been reported to form by ammonium precipitation [41] [42] .

Table 1. Textural properties of studied catalysts.

Sample	Ni loading (%)	Promoter loading (%)	S_{BET} (m^2 g^{-1})	t-plot micropore area (m^2 g^{-1})	t-plot external surface area (m^2 g^{-1})	t-plot pore volume (cm^3 g^{-1})	Avg. pore diameter (nm)
Bare AC	-	-	193	72	121	0.044	15.5
5Ni	5.4*	-	180	59	121	0.031	18.0
10La	-	-	73	3	70	0.001	27.6
5Ni10La	4.8*	10.3*	61	17	44	0.009	32.8
10Nb	-	-	203	70	133	0.041	15.1
5Ni10Nb	5.4*	8.3*	178	53	125	0.028	18.7

* Leaching of metallic species into the liquid phase following activity tests was determined to be negligible with <5 mg L^{-1} for Ni and <0.5 mg L^{-1} for La and Nb by ICP-OES analysis

SEM images of reduced and spent catalysts are presented in Figure 1. By external observation of the SEM images, it appears that all three catalysts used in this study are analogous and demonstrate homogenous dispersion across the support after reduction at 400 °C. No major alterations were perceived in catalyst structure or dispersion after reduction or in spent catalysts following activity tests, suggesting that particle coarsening and/or coking was minimal under the conditions implemented in this study.

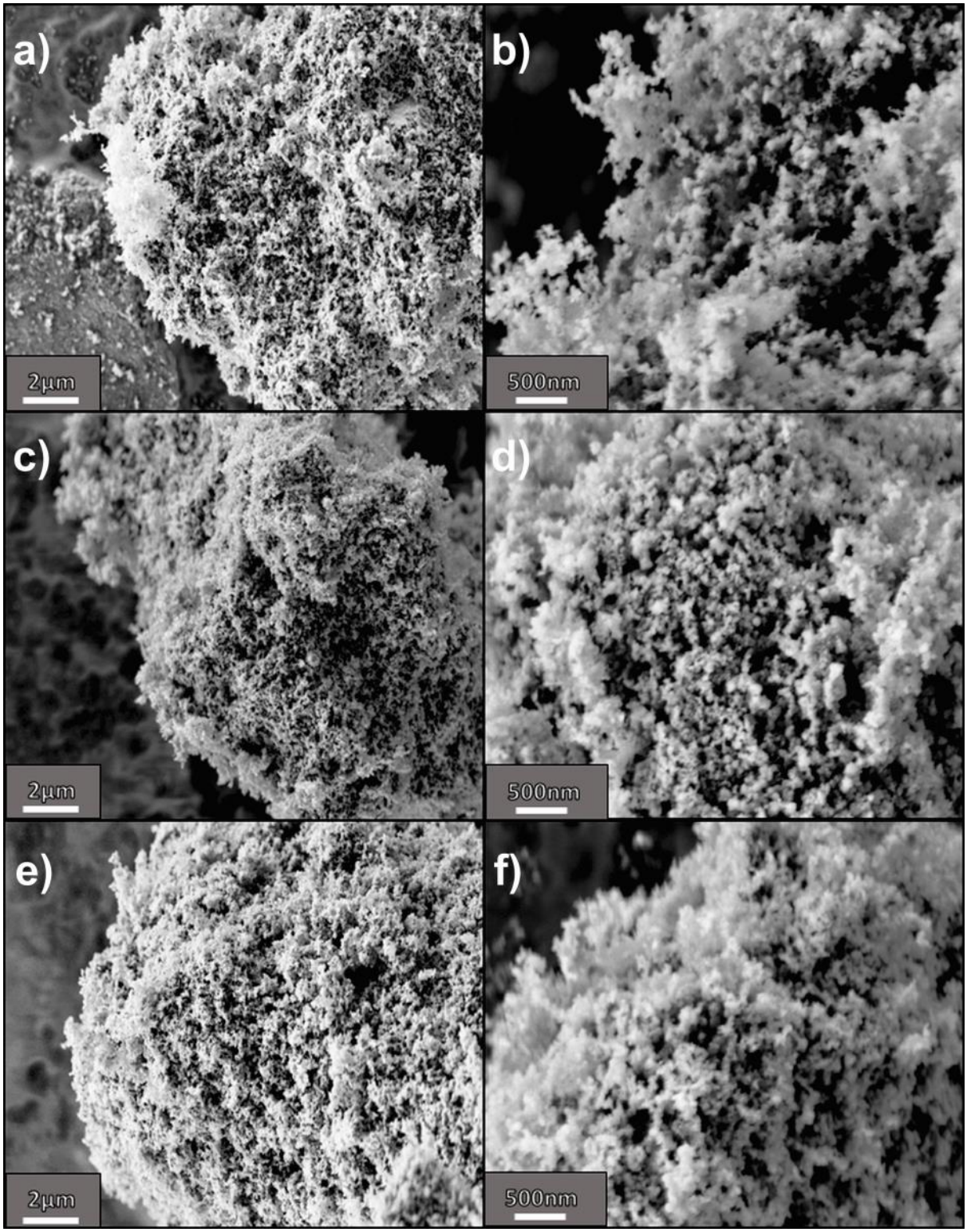

Figure 1. SEM images of carbon-supported 5Ni (a-b), 5Ni10La (c-d), and 5Ni10Nb (e-f) of reduced (a,c,e) and spent (b,d,f) catalysts.

TEM was performed to observe surface and textural properties in more detail compared to SEM, and images are displayed in Figure 2. Figure 2a and 2b of reduced

catalysts demonstrate that the high dispersion of metal particles appears to be relatively retained during the reduction process at elevated temperatures with minimal particle growth or agglomeration into larger particles. The bimetallic catalysts NiLa and NiNb were determined to have a significantly smaller average particle size with a d_{NTEM} of 8 nm and 7 nm respectively, compared to 11 nm of the Ni catalyst, indicating that nickel particle dispersion was likely improved from the promotion of La and Nb as originally hypothesized. Figure 2c captured individual nickel particles on the Ni catalyst surface approximately 5-8 nm in size. The spent 5Ni catalyst shown in Figure 2d suggests that individual nickel particles preserve their distinctiveness following reduction and catalytic testing, in alignment with the nearly equal average particle size observed (d_{NTEM} of 10 nm) relative to reduced Ni catalyst prior to activity tests (d_{NTEM} of 11 nm).

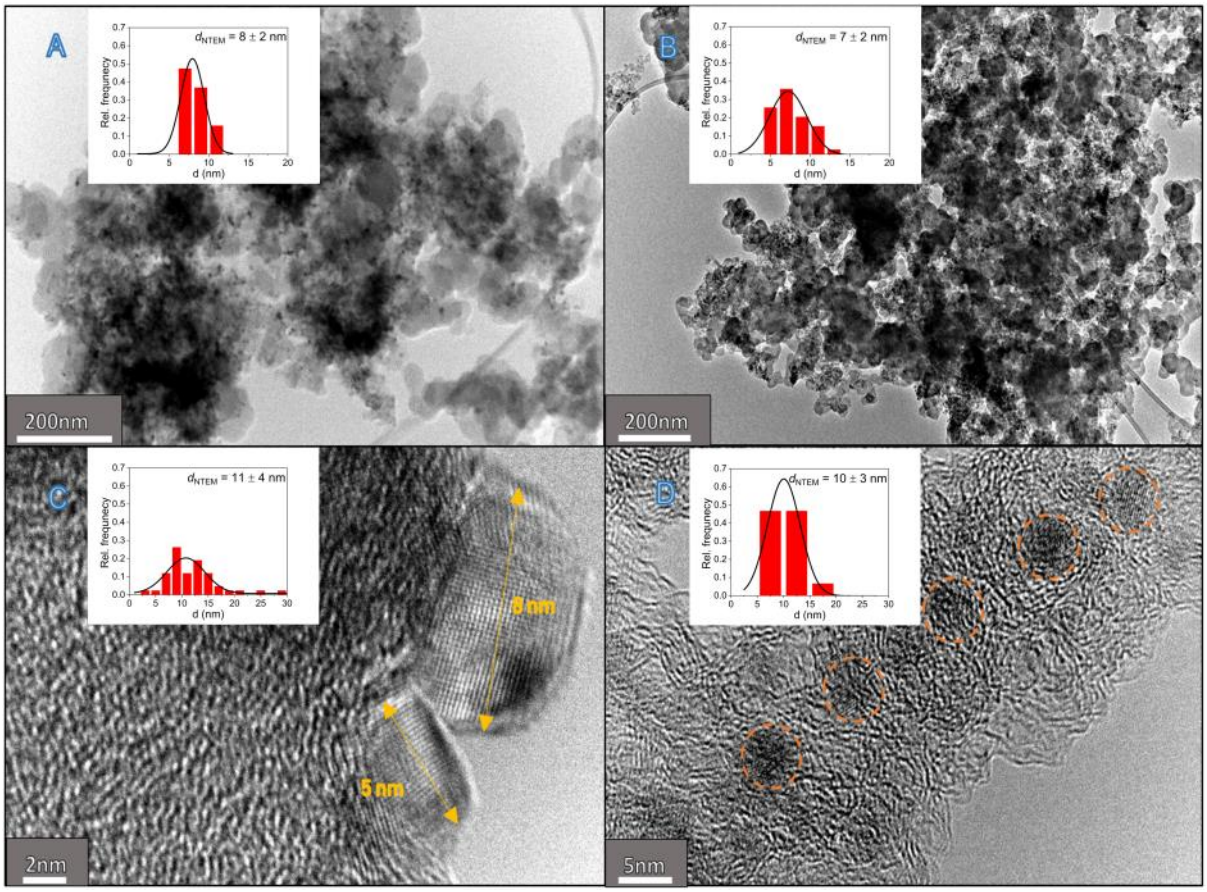

Figure 2. TEM images of a) reduced NiLa b) reduced NiNb c) reduced Ni and d) spent Ni.

XRD profiles for fresh and reduced carbon-supported catalysts are displayed in Figure S.3 (Supplementary Material). The broad diffraction peak at 2Θ = 25° detected for all catalysts has been associated with (002) plane of amorphous coke-like structures that are present as disordered, carbonaceous layers in the carbon support [44] [45]. The diffraction peak at 2Θ = 44° corresponds to (100) plane, owing to crystalline carbon within the support [46] [47]. Due to the nature of the carbon, which generated wide and intense diffraction peaks, especially after reduction, it is not possible to precisely identify the presence of explicit metallic phases or the formation of mixed oxides of Ni with La or Nb species.

XPS analyses were performed on three samples. Elements C, O, Ni, Nb and La were detected on the surface of these samples. High energy resolution Ni 2p, Nb 3d and La 3d spectra were acquired and are shown in Figure 3 in Supplementary Material. The Ni 2p spectra from samples 5Ni and 5Ni10Nb are similar (Figure 3a and 3b). The Ni $2p_{3/2}$ peaks consist of three components. The peak at 852.7 eV is assigned to metallic Ni(0) and the peak at 855.8 eV is assigned to Ni(3+) in Ni_2O_3-like compound [48]. There is also a Ni-satellite peak at 861.4 eV related with Ni(3+). Unfortunately, Ni 2p spectrum from 5Ni10La sample is overlapping with La 3d spectra (Figure 3d) and it cannot be used for identification of oxidation state of Ni in this sample [49]. In sample 5Ni10Nb, the XPS spectrum Nb 3d (Figure 3c) has a main peak Nb $3d_{5/2}$ at 207.7 eV and it is assigned to Nb_2O_5-like environment [48]. No metallic Nb at 202 eV was detected in this spectrum at 202 eV. In sample 5Ni10La the XPS spectrum La $3d_{5/2}$ (Figure 3d) has a double structure, where La $3d_{5/2}$ peaks are at 834.7 and 838.3 eV [49]. This double structure is assigned to La-oxide. No metallic La was identified in this spectrum.

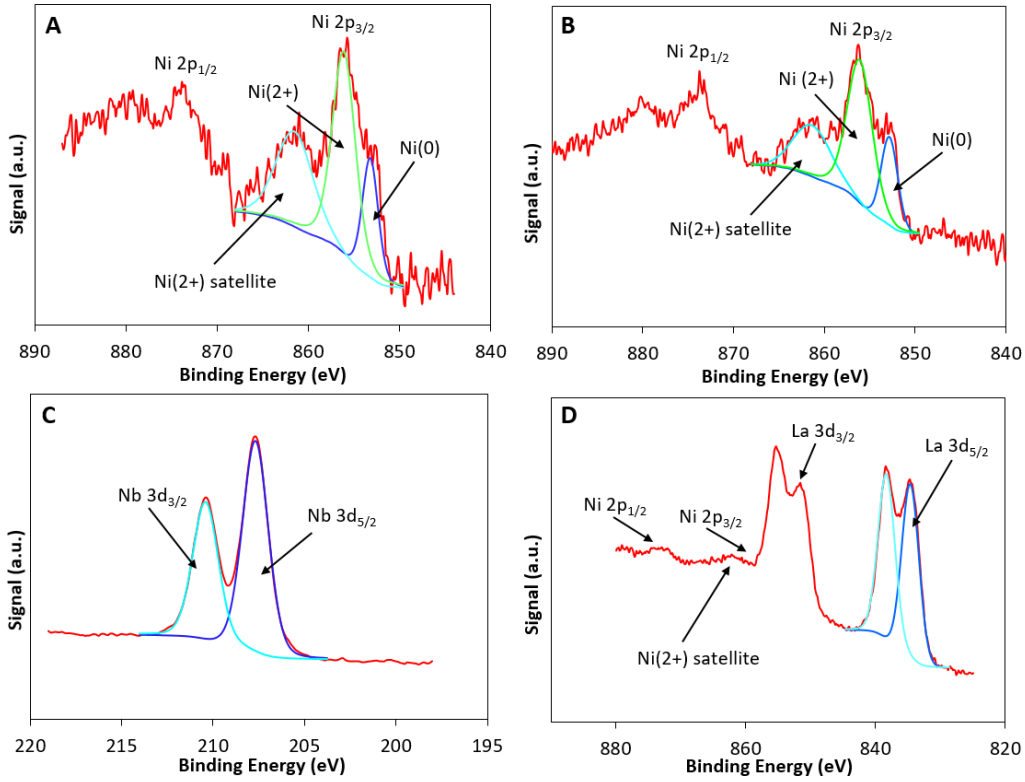

Figure 3. XPS Ni 2p of reduced 5Ni (A) and reduced 5Ni10Nb (B). XPS Nb 3d of reduced 5Ni10Nb (C). XPS Ni 2p and La 3d of reduced 5Ni10La.

3.1.2 Hydrogen temperature programmed reduction

H_2-TPR is an important method that can identify the optimal reduction temperature that activates a maximum amount of metal while restricting the amount of sintering that can occur at elevated temperatures [50]. H_2-TPR profiles for bare AC support, La and Nb-doped activated carbon without Ni, and nickel and lanthanum oxides are presented in Figure 4 for comparative purposes. An initial reduction test was conducted on the bare activated carbon support indicating negligible reducibility. A slight negative shoulder is observed at higher temperatures beginning at 600 °C. This is attributed to CO desorption from thermal decomposition of the oxidized carbon surface as oxygen chemisorbed onto carbon is frequently reported [51]. Literature commonly reports the irreducible nature of lanthanum

oxides (La_2O_3) which can be clearly observed in Figure 4 with no detectable H_2 uptake [38]. Therefore, the peak detected for La-doped AC at ~500 °C has been described to correspond to the decomposition of readily formed lanthanum oxycarbonates ($La_2O_2CO_3$) or hydroxycarbonates ($LaOHCO_3$), not corresponding to any reduction capability [52–54]. This was further confirmed by performing H_2-TPR-MS on the La-doped AC catalyst which detected the presence of CO (m/z = 28) and CO_2 (m/z = 44) (Figure S.6). H_2-TPR profile of Nb-doped catalyst indicated, although rather minor, two reduction peaks at ~585 °C and ~860 °C. The first peak is associated with the reduction of superficial NbO_x species [55,56]. The second peak at 860 °C is attributed to the partial reduction (Nb^{+5} → Nb^{+4}) of bulk Nb_2O_5 phase to NbO_2. [57–59]. The complete reduction to NbO (Nb^{+4} → Nb^{+2}) is reported in the literature to occur at much higher temperatures (~1300 °C) which was not possible to achieve under these implemented TPR parameters [39,40]. Finally, pure NiO was also subjected to reduction for comparative purposes and a major peak was observed between 240 °C and 400 °C, attributing to the complete reduction of NiO (Ni^{+2} directly to Ni^0) [60]. Based on these results, 400 °C was selected as an optimal reduction temperature for catalytic activity tests as it would reduce the vast majority of NiO species in all Ni-containing catalysts.

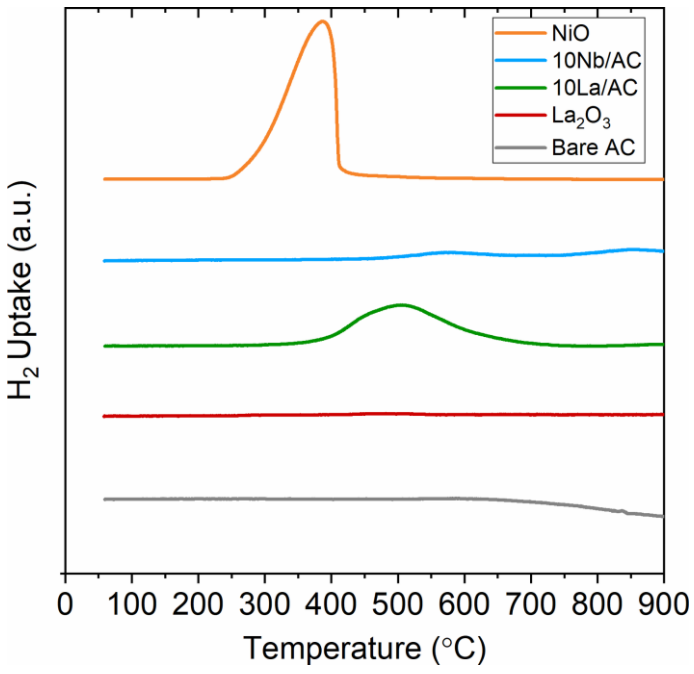

Figure 4. Comparative H_2-TPR profiles of bare support, metal oxides, and Ni-free doped AC.

Table 2. Quantitative results for total hydrogen consumption and for each deconvoluted peak.

Sample	T_{max} (°C)	H_2 Consumption [a] (mmol g^{-1})	H_2 Consumption below 400 °C (%)	Total H_2 Consumption (mmol g^{-1})
5Ni	218	0.008	41	0.230
	281	0.062		
	357	0.046		
	478	0.106		
	681	0.007		
5Ni10La	315	0.174	66	0.227
	450	0.064 [b]		
	797	0.053		
5Ni10Nb	312	0.057	41	0.153
	344	0.031		
	367	0.019		
	515	0.017		
	690	0.030		

[a] Experimental error for hydrogen consumption during H_2-TPR was determined to be ±5%.
[b] Excluding the peak representing LaO_2CO_3/ $LaOHCO_3$ identified in 10La/AC in Figure 4.

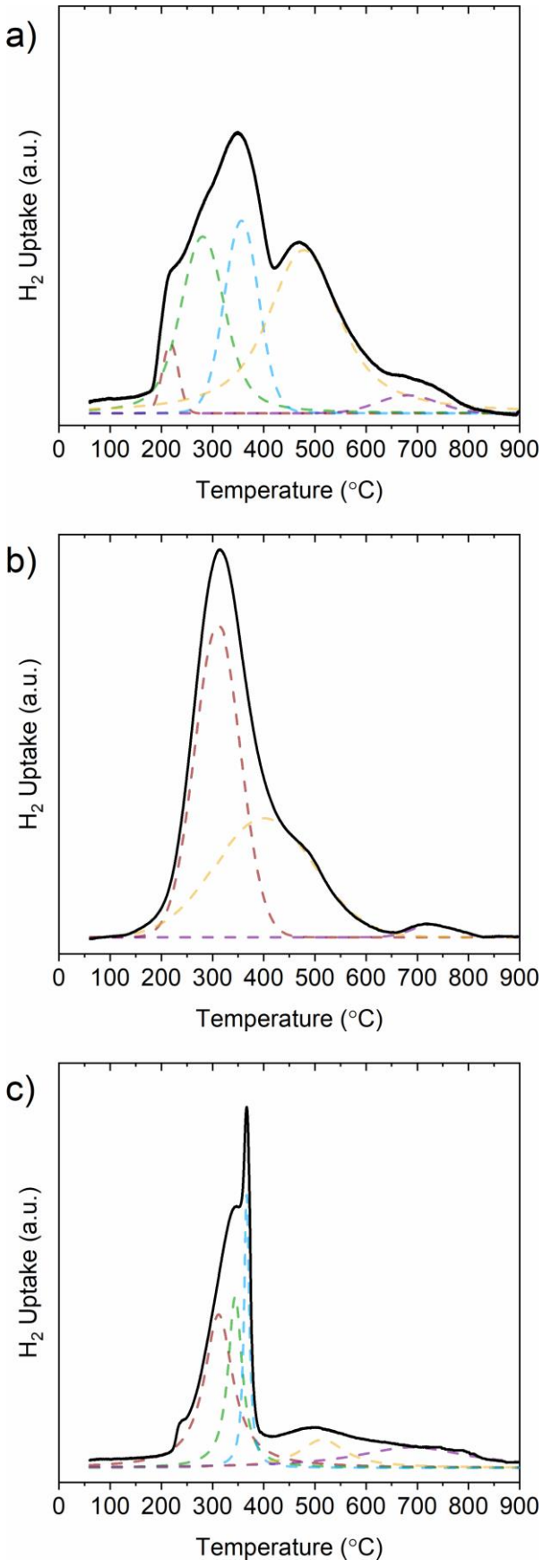

Figure 5. Deconvoluted H_2-TPR profiles of a) 5Ni, b) 5Ni10La, and c) 5Ni10Nb.

Broad H_2-TPR profiles for catalysts containing Ni were then deconvoluted into symmetrical peaks to further investigate the individual NiO species and provide more detailed information on catalysts reducibility. Deconvolution was carried out via Origin software using Lorentzian multi-peak curve fitting and are presented in Figure 5. Quantitative results for overall hydrogen consumption as well as each deconvoluted peak are shown in Table 2. The deconvoluted H_2-TPR profile for 5Ni (Figure 5a) indicate the presence of several overlapping elemental reduction progressions between 150 °C – 800 °C due to altering strengths of interaction with surface functional groups on the activated carbon support [61]. The first 3 bands can be associated as follows; peak I at 218 °C is related to well dispersed NiO species that are interacting weakly with the AC support and are the most readily reduced, peak II at 281 °C is also associated with moderately dispersed nickel, and peak III at 357 °C is associated with bulk NiO that is more strongly interacting with the support [62–64]. The harder to reduce peak IV at 478 °C and peak V at 681 °C are not present in the TPR of pure NiO and are likely intensely interacting with functional groups on the surface of the support. This correlates well with the H_2-TPR profile of the bare AC (Figure 4) as oxygen-containing functional groups such as phenolics, quinones, and carbonyls are not thermally stable above 600 °C [65]. Furthermore, these functional groups may affect the distribution or occurrence of neighbouring oxygen surface vacancies to NiO when in tight contact with the carbon support, which is presumed to be the initiating factor for NiO reduction [60,66].

Figure 5b of 5Ni10La deconvoluted H_2-TPR profile resulted in a significant shift in reduction to lower temperatures with a major peak at 315 °C. Relative to 5Ni, it appears that NiO dispersion was substantially improved and more uniformly distributed as the reduction peak(s) corresponding to dispersed NiO is much more pronounced and bulk NiO appears to be almost non-existent. Total hydrogen consumption remained relatively equal with

0.230 mmol g^{-1} for 5Ni and 0.227 mmol g^{-1} when lanthanum was initially impregnated, however the percentage below 400 °C varied greatly with 41% and 66%, respectively. This aligns well with literature that reports the capability of lanthanum to lessen the interaction between metal-support by forming a layer on the surface of the support, and possibly forming La-Ni oxides [19,21]. The drop in surface area and pore volume observed during N_2 adsorption in Table 1 also confirms this probable covering of the support by lanthanum. Furthermore, lanthanum addition also has been described to improve the stability of nickel by preventing sintering/agglomeration into larger, less dispersed Ni particles at elevated temperatures during reduction [20,67].

Alternatively, niobium addition compressed the reducibility of nickel which positioned sharply around 360 °C as shown in Figure 5c. H_2-TPR analysis indicates that niobium diminished the amount of well dispersed NiO (peaks I and II) relative to the amount of bulk NiO species with a stronger interaction with the support. Interestingly, contrary to the influence of lanthanum, niobium significantly decreased the overall H_2 consumption from 0.230 mmol g^{-1} to 0.153 mmol g^{-1}, although most of this loss in H_2 consumption corresponds to nickel species strongly interacting with the support (>400 °C). This suggests niobium likely deteriorates the strong interaction between nickel and the support by forming a layer over the activated carbon. Some studies have reported Nb to embed itself into and weaken the Ni-O-Ni lattice bonds resulting in a lower NiO reduction temperature, but this was not observed in this case [23,68]. It is possible that the higher portion of bulk NiO and diminished H_2 consumption transpires due to niobium oxides partially encompassing NiO particles which has been mentioned elsewhere, hindering their reducibility [25].

3.2 Acid and Metal Sites Determined by NH_3-TPD and CO-TPD

Ammonia temperature-programmed desorption coupled with a mass spectrometer (NH_3-TPD-MS) was performed on catalysts to determine total acidity and relative strength of acid sites by quantification of desorbed ammonia. The mass spectroscopy signals displayed in Figure 6a are from m/z = 15 to isolate desorbed ammonia from water (both have mass spectrums of m/z = 17). Diffuse reflectance infrared Fourier transform (DRIFT) FTIR technique was attempted on the catalyst samples but no conclusive information could be obtained about the type of acid sites present due to the poor transmittance nature of the activated carbon support. An initial NH_3-TPD test was conducted on bare AC support and its profile concluded negligible acidity contribution. All doped-catalysts indicated very low overall acidity corresponding to very weak acid site strength, desorbing from as low as 75 °C up to 350 °C. The 13 µmol g^{-1} of acid sites determined for 5Ni catalyst is associated with the Lewis acidic nature typical of Ni^{2+} sites [69,70]. The NH_3-TPD profile for lanthanum-containing catalysts also indicated the presence of weak acid sites, likewise Lewis acid sites from La^{3+} oxidation state [71,72]. Compared to 5Ni, the NH_3-TPD profile for 5Ni10Nb catalyst confirms more than five times the amount of acid sites with seemingly slightly stronger character relative to only Ni. Niobium can yield both Lewis acid sites, in the form of Nb=O bonds, and Brønsted acid sites in the form of Nb-OH groups, which would be expected to be more prevalent following reduction in a hydrogen environment [73,74].

Carbon monoxide – temperature programmed desorption coupled to a mass spectrometer (CO-TPD-MS) was conducted to determine CO chemisorption and quantified to estimate the concentration of metallic active sites on the catalyst surface, shown in Table 3, and mass spectrum signals associated with CO (m/z = 28 with deduction from CO_2 contribution) are displayed in Figure 6b. Mass spectrums corresponding to CO_2 (m/z = 44) are also shown in Figure 6c. Although determined to be irreducible, 10La catalyst resulted in

significant CO desorption starting around 450 °C owing to metallic active sites. With 5Ni10La catalyst, after deducting the contribution from lanthanum, resulted in approximately two times as many metal sites with 345 μmol g^{-1} relative to the 5Ni catalyst. This correlates well with the improved reducibility observed during H_2-TPR and related studies that have reported increased nickel dispersion with lanthanum promotion [19–21]. Alternatively, the niobium-doped catalyst contributed very few metallic sites with only 19 μmol g^{-1}, resulting in almost equal metallic sites between 5Ni and 5Ni10Nb catalysts, after deducing contribution from Nb, with 160 μmol g^{-1} and 180 μmol g^{-1}, respectively. Carbon dioxide formation during CO-TPD with 5Ni10La catalyst was ~400% and ~800% higher in comparison to 5Ni and 5Ni10Nb catalysts, respectively, and thus its contribution had to be considered when determining total metallic sites. The production of CO_2 during CO-TPD has been regularly described to occur via a Mars-van Krevelen mechanism where CO reacts with the oxygen atoms within the lattice of the metal oxides present, leading to oxygen vacancies on the catalyst surface [75,76].

Table 3. Quantitative results for NH_3 and CO desorption and total concentration of sites.

Sample	Volume of NH_3 (mL)	Conc. Of Acid sites (μmol g^{-1})	Volume of CO (mL)	Conc. Of Metal Sites (μmol g^{-1})	Volume of CO_2 (mL)
5Ni	0.031	13	0.365	160	0.057
10La	0.193	86	0.330	144	0.206
10Nb	0.234	105	0.041	19	0.013
5Ni10La	0.043	19	1.03	489	0.267
5Ni10Nb	0.224	96	0.447	199	0.032

Experimental error for NH_3, CO, and CO_2 desorption was determined to be ±10%

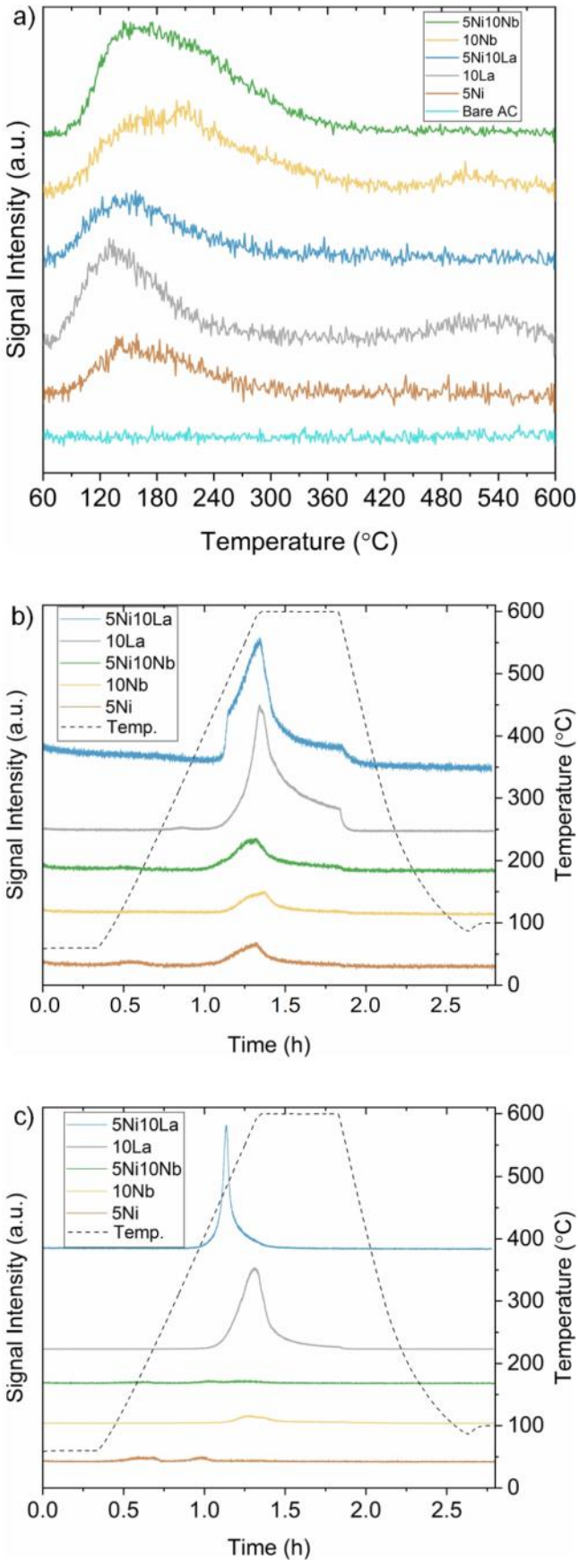

Figure 6. TPD-MS profiles for a) NH_3-TPD-MS (m/z = 15), b) CO-TPD-MS profiles (m/z = 28), c) CO-TPD-MS profiles (m/z = 44) for all catalyst samples.

3.3 Reaction pathway network and microkinetic model development

Before the model development, a detailed reaction pathway has been proposed as shown in Figure 7 that is based on all detected intermediates and products during catalytic activity tests. The colours of each compound displayed in the reaction network match the colours presented later in Figures 7-9 that display concentration profiles. Tetrahydro-5-methylfuran-2-methanol (MTHFA) in grey has been reported in other studies but was not detected under these experimental conditions.

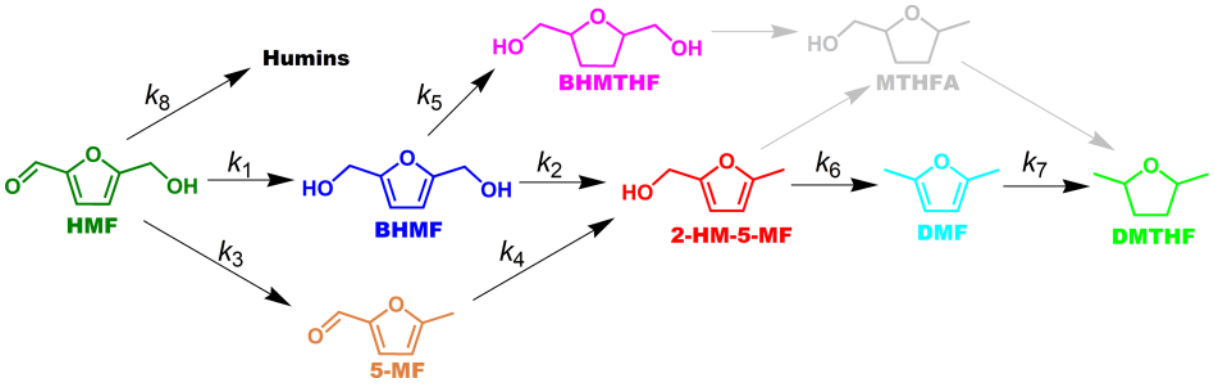

Figure 7. Observed (colours) and alternative (grey) reaction network of HDO of HMF.

The model intends to describe a three phase system that considers a hydrogen solubility being in the thermodynamic equilibrium at the gas-liquid interface, competitive adsorption and desorption of all components on/from the catalyst surface, and their catalytic transformation on the catalyst surface. Modelled concentration and catalyst coverage values for each component were calculated by solving a set of ordinary differential equations based on the proposed reaction pathway stated above, with regard to the following assumptions;

1) Based on experiments performed with blank AC support (shown in Figure 8f) resulting in negligible activity, it is assumed that all reactions are heterogeneous occurring on the catalyst surface,

2) Surface reactions are considered to exclusively transpire only on metallic sites. Experiments conducted with 10Nb and 10La on AC (shown in Figures 9f and 10f) resulting in negligible activity justify the implementation of this assumption that reactions are undeniably dependent on metallic sites. Therefore adsorption, desorption, and surface coverages of both organic compounds and hydrogen were only considered to occur on metallic sites,
3) Vacant sites relevant for adsorption are all equivalent and independent of the overall coverage,
4) Each active (metal) site is covered by one organic or hydrogen molecule at a time as they absorb competitively,
5) Adsorption and desorption constants of all organic products are considered equivalent due to their similar structure,
6) Hydrogen solubility in THF was linearized from previously reported Henry constant values to fit the reaction conditions implemented in this study (170 – 230 °C and 5 MPa of H_2) [77],
7) Since the initial large H_2 pressure of 5 MPa, concentrations of other (initially liquid) products in the gas phase were considered to be negligible and their balances were not included in the set of ordinary differential equations in this work,
8) Humin formation was presumed to follow what has been reported in the literature and its concentration was estimated to equate to the concentration of the unaccounted carbon balance [78]. For simplicity in the model, humin formation was considered to be limited to dimers and not larger oligomers.

Adsorption rate (r_j^{ads}) of each compound *j* depends on the adsorption rate constant (k^{ads}), its concentration in liquid phase (C_j^L), and concentration of vacant sites (Θ_{VS}), defined in Eq. 1

$$r_{\mathrm{j}}^{\mathrm{ads}} = k_{\mathrm{j}}^{\mathrm{ads}} C_{\mathrm{j}}^{\mathrm{L}} \Theta_{\mathrm{VS}} \quad (1)$$

Desorption rate ($r_{\mathrm{j}}^{\mathrm{des}}$) of each compound *j* depends on the desorption rate constant (k^{des}), and coverage of *j* adsorbed to active sites (Θ_{j}), defined in Eq. 2.

$$r_{\mathrm{j}}^{\mathrm{des}} = k_{\mathrm{j}}^{\mathrm{des}} \Theta_{\mathrm{j}} \quad (2)$$

Surface reaction rate ($r_{\mathrm{i}}^{\mathrm{surf}}$) of each reaction *i* depends on the surface reaction rate constant (k^{surf}) and coverage of corresponding reactant *j* (Θ_{j}) and hydrogen (for hydrogenation and HDO reactions) adsorbed to active sites, defined in Eq. 3.

$$r_i^{surf} = k_{\mathrm{i}}^{surf} \Theta_{\mathrm{j}} \Theta_{\mathrm{H}} \quad (3)$$

The kinetic model accounts for not only the isothermal segment of the process at final temperature but also the initial heating-up of reaction mixture to the desired reaction temperature. Temperatures and pressures recorded during every experiment were used for each time step to calculate mass transfer constants, reaction rate constants, and thermodynamic properties like equilibrium hydrogen solubility, while both adsorption and desorption rate constants were considered independent of temperature and orders of magnitude higher than the (rather low) reaction rate constants. The influence of temperature on rate constants for surface reactions was employed to follow Arrhenius law as presented in Eq. 4;

$$k_{\mathrm{i}}^{\mathrm{surf}}(T_2) = k_{\mathrm{i}}^{\mathrm{surf}}(T_1) \times \exp\left(\frac{Ea_{\mathrm{i}}}{R}\left(\frac{1}{T_1} - \frac{1}{T_2}\right)\right) \quad (4)$$

Differential balance equations based on the proposed reaction network (Figure 7) and Eq. 5-8 were implemented as follows;

General balance for H_2 concentration $C_{\mathrm{H2}}^{\mathrm{G}}$ in the headspace volume of the reactor (V_G), where $k_{\mathrm{GL}}a$ dependence on the stirring speed in this type of reactor was adopted from our previous work [79]:

$$\frac{dC_{H2}^{G}}{dt} = -k_{GL}a\left(\frac{p_{H2}}{H} - C_{H2}^{L}\right)\frac{V_L}{V_G} \quad (5)$$

General balance for liquid phase, where n_{TS} is the surface concentration of metal sites and V is the volume of the liquid phase:

$$\frac{dC_j^L}{dt} = -r_j^{ads} + r_j^{des}\frac{n_{TS}}{V} \quad (6a)$$

General balance for concentration of H_2 in liquid phase:

$$\frac{dC_{H2}^{L}}{dt} = +k_{GL}a\left(\frac{p_{H2}}{H} - C_{H2}^{L}\right) - r_j^{ads} + r_j^{des}\frac{n_{TS}}{V} \quad (6b)$$

General balance for coverage of active sites:

$$\frac{d\Theta_j}{dt} = r_j^{ads}\frac{V}{n_{TS}} + r_j^{des} + \sum_i^I \pm r_i^{surf} \quad (7)$$

For all the reactions *i*-s (*I* is their number) that consume or form *j*. The vacant active site coverage was balanced with the consideration of Eq. 8.

$$\frac{d\Theta vs}{dt} = \sum_j^J r_j^{ads}\frac{V}{n_{TS}} + \sum_j^J r_j^{des} + \sum_i^I(\pm r_j^{surf}) \quad (8)$$

For all compounds *j*-s (*J* is their number) that adsorb or desorb and for all reactions *i*-s (*I* is their number) that have unstoichiometric balance of sites. If the reactant-product molar ratio is always 1-1 or 2-2, then the last sum can be omitted.

Concentration profiles were modelled by a set of ordinary differential equation (ODE) solved with Runge-Kutta (2,3), based on the Matlab solver used. Initial concentrations of all components were set at zero, excluding the starting reactant (HMF) in the liquid phase, hydrogen partial pressure in the gas phase (calculated by Henry law). To the best of our knowledge, the solubility of hydrogen in tetrahydrofuran has been measured only by Brunner [77] which was used in the calculation of Henry's constant in Eq. 9 and application in Eq. 6b, where H denotes Henry's constant defined via concentration, p_{H2} is the partial pressure of hydrogen in the gas phase and c_{H2} stands for the concentration of hydrogen in the solvent,

hence reaction mixture. Brunner provided phase-equilibrium and the obtained Henry's constant showed exponential dependence on temperature in the form of

$$H = 2544.132 \times e^{-0.007272 \cdot T} \quad (9)$$

The total concentration of active sites on the catalyst surface (Θ_{VS}) were determined independently by CO-TPD chemisorption (see Table 3).

$$f\left(k_{i-j}, Ea_{i-j}\right) = \sum (C_{exp} - C_{mod(k_{i-j}, Ea_{i-j})})^2 \quad (10)$$

Nelder–Mead method was used for coarse regression of all experiments with the same catalyst type simultaneously by minimization of the objective function (Eq. 10), whereas Levenberg–Marquardt method was used for fine regression analysis and to calculate Jacobian matrix and 95% confidence intervals.

Turnover frequencies (TOF) for each catalyst were calculated using the general equation;

$$TOF = k_{\mathrm{i}}^{\mathrm{surf}} \Theta_{\mathrm{j}} \Theta_{\mathrm{H}} \quad (11)$$

Where a constant maximum reaction temperature of 230 °C and equivalent initial concentrations of each reactant *j* were applied for best comparative purposes.

3.4 Catalytic Activity Tests and Modelled Results

Liquid products analyzed by GC-MS for 5-hydroxymethylfurfural HDO over nickel-based activated carbon catalysts under our reaction conditions established the most foremost intermediates and products to be; 2,5-bis(hydroxymethyl)furan (BHMF), 2,5-bis(hydroxymethyl)tetrahydrofuran (BHMTHF), (5-methyl-2-furyl)methanol (2-HM-5-MF), dimethylfuran (DMF), dimethyltetrahydrofuran (DMTHF), and 5-methylfurfural (MF). 5-methyltetrahydro-2-furanyl methanol (MTHFA) was not detected in this study but has been reported elsewhere using similar nickel-carbon catalysts [36,80]. Based on these detected products, a reaction pathway is presented in Figure 7 in which the kinetic model relies on.

Experimental (symbols) and modelled (lines) concentrations in the liquid phase as a function of time for reaction temperatures between 170 °C−230 °C are shown in Figures 8-10 and their corresponding kinetic parameters based on regression analysis are presented in Table 4.

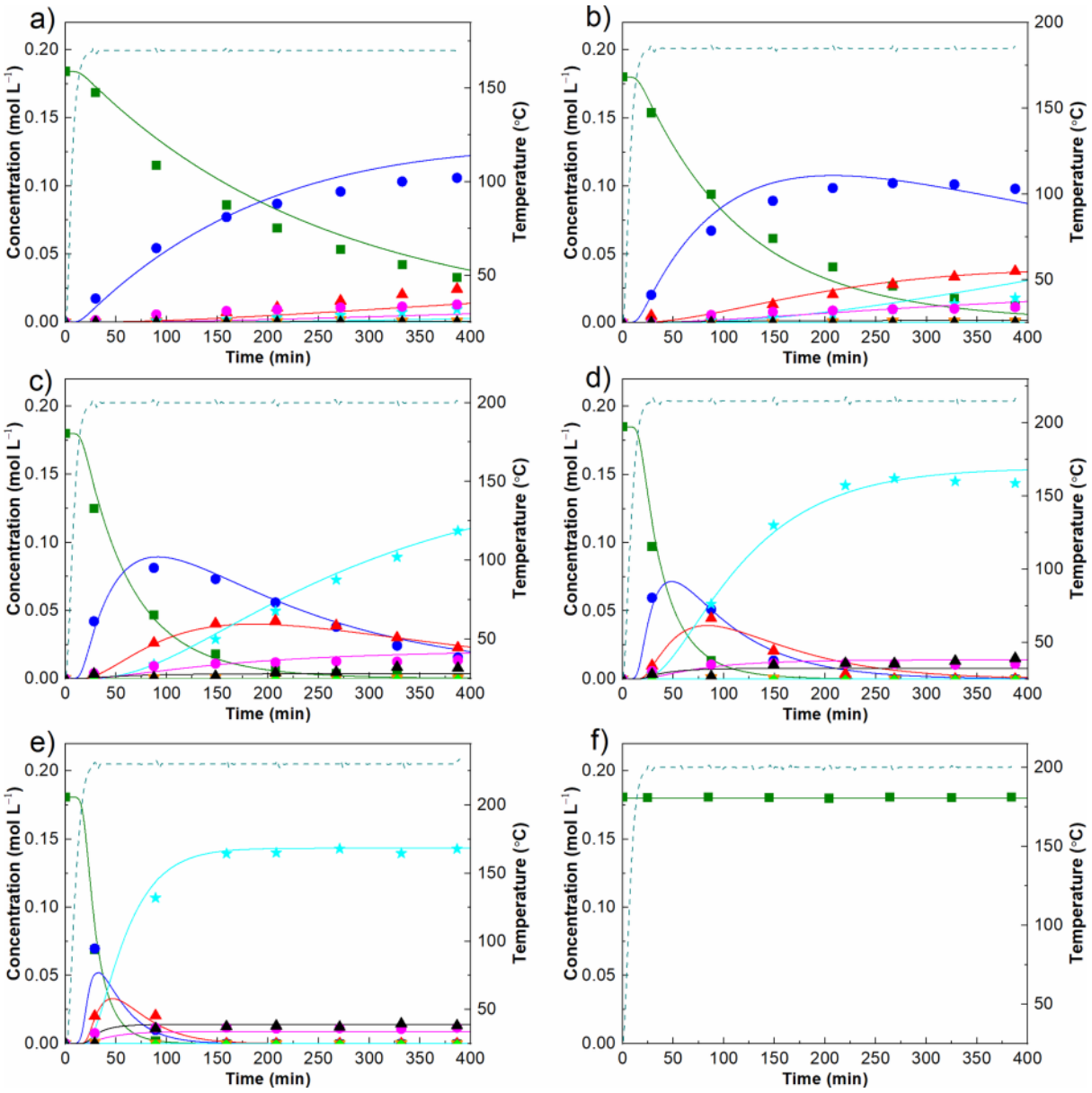

Figure 8. Temperature influence on product distribution over time using 5Ni/AC at a) 170 °C, b) 185 °C, c) 200 °C, d) 215 °C, e) 230 °C, and f) blank AC at 200 °C. ■ HMF, ● BHMF, ▼ 5-MF, ▲ 2-HM-5-MF, ★ DMF, ● BHMTHF, ◆ DMTHF, ▲ Humins. - - - Temperature. Model values correspond to lines, experimental values correspond with symbols.

At lower temperatures <200 °C, catalytic tests with 5Ni resulted in BHMF as the major product (57% and 54% at 170 °C and 185 °C, respectively), 2-HM-5-MF as the

secondary product (13% and 21%, respectively) with trace amounts of DMF and BHMTHF. As the reaction temperature was increased to 200 °C, DMF production began to prevail at 215 minutes with a final product selectivity around 60% after the full reaction time. At reaction temperatures above 200 °C, DMF production dominated with 78% selectivity and nearly complete conversion after only 2 hours from initial heating. According to rate constants shown in Table 4, evidently for 5Ni catalyst, the highest rate constant is k_1 of 60.9 min^{-1}, indicating that the first reaction involving the reduction of the aldehyde occurs relatively fast. Activity tests performed with blank AC (Figure 8f), and Nb/La-doped support (Figure 9f and 10f, respectively) that demonstrated trivial activity also demonstrate that k_1 is highly reliant on the presence of nickel metallic sites and cannot proceed without them. Nickel has been well-established as a suitable hydrogenation catalyst for the hydrogenation of carbonyl groups where the reduction of aldehydes to alcohol is relatively easy compared to other carbonyl groups such as ketones and esters [81–83]. This reaction can occur by either hydrogen attack to the O or C atom of the carbonyl group, though it has been suggested that the former is more preferred due to the stabilization the furan ring provides for the hydroxyalkyl intermediate [84,85].

Conversely, the primary dehydration of BHMF to yield 2-HM-5-MF (k_2) is approximately a third that of k_1 with 23.3 min^{-1} whereas the second and final dehydration to yield DMF (k_6) occurred relatively faster with 37.2 min^{-1}. The related TOF values calculated at 230 °C was almost double for the second dehydration step relative to the first with 7.23 min^{-1} and 4.56 min^{-1}, respectively. These reaction rate constants signify 2-HM-5-MF formation (k_2) to be the rate-limiting step in the major reaction pathway towards complete deoxygenated DMF. This is likely due to the low acidity of the 5Ni catalyst (as shown in Table 3) since hydrodeoxygenation reactions generally encompasses bifunctional metal-acid catalysts that provide dehydration function via acid sites whereas metal sites are involved in

hydrogenation reactions. Strong acid sites alone could not catalyze this reaction, as shown in Figure 10f with 10Nb, demonstrating the constraint for the synergistic effects of both metal and acid sites for effective hydrodeoxygenation.

The alternative reaction pathway associated with the direct dehydration to yield 5-MF (k_3 and k_4) were significantly slower than the main reaction pathway with <0.1 min^{-1} and 0.2 min^{-1}, respectively. Due to the moderately high bond dissociation energies of the C–OH group to be around 280 kJ mol^{-1}, it seems logical that the direct dehydration to 5-MF while keeping the aldehyde group intact would not readily occur [86] [87]. The side reaction involving the formation of humins (k_8) was also quite slow with 1.4 min^{-1}, although was not insignificant with a final product selectivity of 7% at 230 °C (Figure 9e).

Minimal furan ring saturation to produce BHMTHF (k_5) occurred and zero DMTHF (k_7) was detected at any reaction temperature. This is likely due to the mode at which the substrates bind to the catalyst where the carbonyl or hydroxyl group adsorb much more strongly, inhibiting any type of flat mode of adsorption with the π electrons of the furan ring [88]. A similar outcome was described in the hydrogenation of furfural where the furan ring was believed to employ a repulsion effect away from Cu atoms on SiO_2 support [89].

The incorporation of La to the nickel catalyst altered the catalyst activity and product selectivity significantly. At reaction temperatures below 200 °C, k_1 involving the reduction of the aldehyde slowed extensively to 7.5 min^{-1} with BHMF being the key product with 42% and 73% product selectivity at 170 °C and 185 °C, respectively. Furthermore, complete HMF conversion was finally achieved only once the reaction temperature reached 215 °C (Figure 9d). Dehydration reaction (k_2 and k_6) yielding 2-HM-MF and DMF, respectively, were both halted to a meagre 0.9 min^{-1} and remained the rate-limiting step in the main reaction pathway. Even when the reaction temperature was 230 °C, complete deoxygenation to DMF was extremely hindered reaching only 11% product selectivity, trivial to the 78%

that was obtained with 5Ni experiments under the same conditions. Humin formation (k_8) was also determined to be negligible.

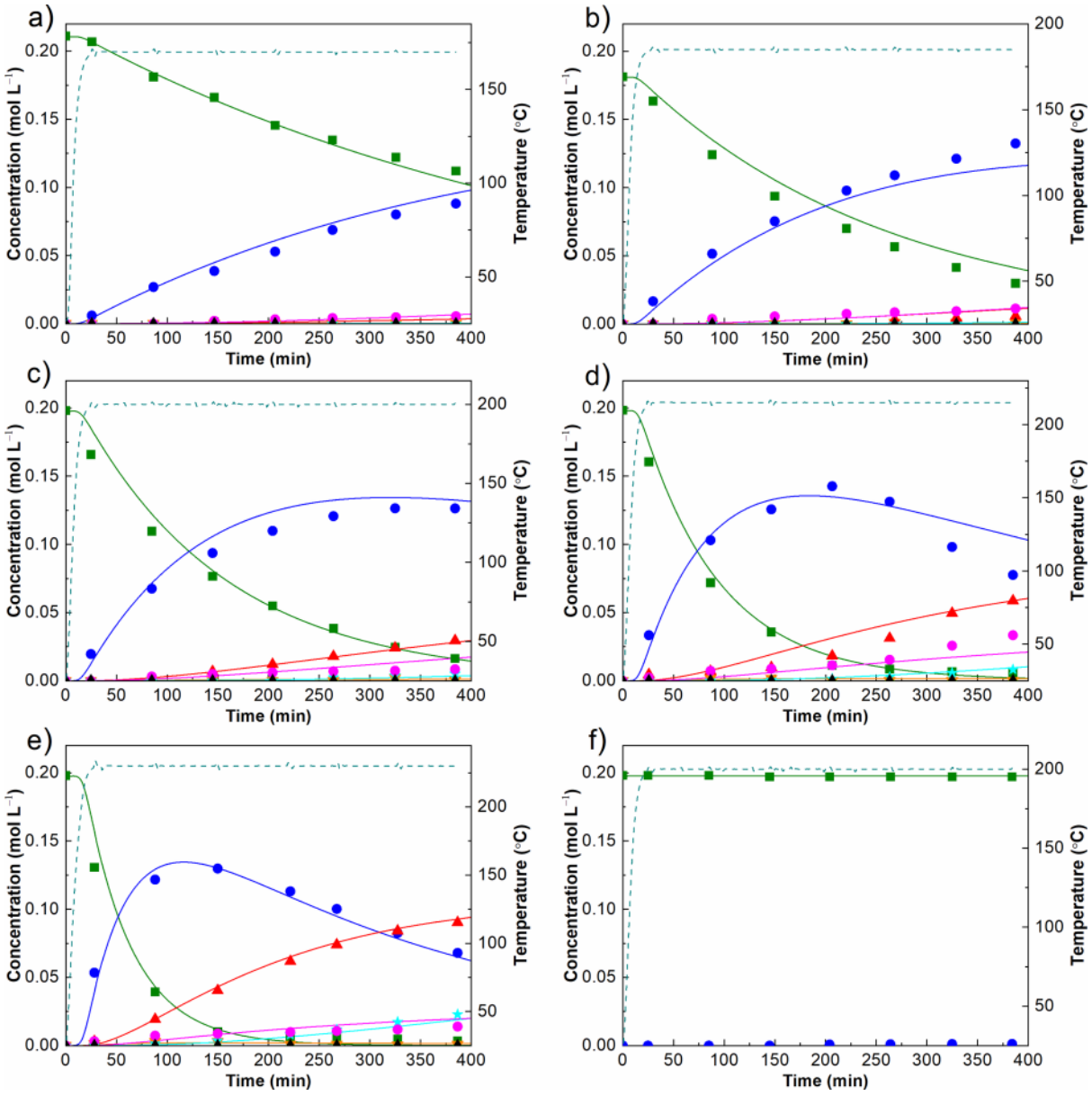

Figure 9. Temperature influence on product distribution over time using 5Ni10La/AC at a) 170 °C, b) 185 °C, c) 200 °C, d) 215 °C, e) 230 °C, and f) 10La at 200 °C. ■ HMF, ● BHMF, ▼ 5-MF, ▲ 2-HM-5-MF, ★ DMF, ● BHMTHF, ◆ DMTHF, ▲ Humins. - - - - Temperature. Model values correspond to lines, experimental values correspond with symbols.

This unexpected drop in activity appeared rather contrary to the improvement in reducibility and increase in available metallic sites that was observed during H_2-TPR and CO-TPD when lanthanum was incorporated into the nickel catalyst. Additionally, activation

energies corresponding to the main reaction pathway towards DMF (k_1, k_2, and k_6) were all determined to be considerably lower compared to 5Ni experiments. Similarly, TOF reduced substantially after lanthanum promotion from 12.94 min^{-1} to 1.75 min^{-1} for k_1 and from 7.23 min^{-1} to 0.20 min^{-1} for k_6. Literature has described the carbonyl group amongst HMF to adsorb via the oxygen atom to Ni metallic sites on the surface of the catalyst [90]. In the absence of lanthanum, the lone pair of electrons provided by the oxygen could be donated to the vacant d-orbital in Ni, enabling strong adsorption of the carbonyl group to the catalyst. Conversely, in the presence of a promoter such as lanthanum which is highly electron dense, Ni would become more electron rich and consequentially, perhaps switch adsorption favourability to hydrogen adsorption rather than the carbonyl group which has been described elsewhere [91,92]. This may explain the increase in reducibility but decrease in activity that was observed. Particle size effects have also been reported to influence adsorption configurations by altering the geometric properties of particles and corresponding active sites (higher content of edge and corner sites on smaller particles)[93]. As determined by particle size distribution diagrams in Figure 2, nickel particles after the initial impregnation of lanthanum are likely smaller in size with a higher content of edge and corner sites, owing to the increase in metallic sites and reducibility that was previously mentioned. In terms of the lower reaction rates and TOF compared to the unpromoted Ni catalyst, Englisch et al. reported similar conclusions with hydrogenation of crotonaldehyde where larger Pt particles favoured the adsorption of the carbonyl group and yielded higher selectivity to alcohols [94]. This was also observed during hydrogenation of furfural where Pt particle sizes >3 nm improved aldehyde reduction to form furfuryl alcohol with a 40-fold increase in TOR compared to smaller particles around 1.5 nm [95]. This influence has been associated with a greater partial positive charge (Niδ+) on larger nickel particles which attracts the oxygen in the carbonyl (or alcohol) group more readily, allowing a more accessible adsorption

configuration [96][97]. Additionally, as determined from N_2 physisorption (Table 1), lanthanum promotion significantly decreased catalyst surface area and total pore volume approximately 3-fold compared to both 5Ni and 5Ni10Nb catalysts, suggesting a large number of pores were blocked. This could have allowed more Ni particles to be dispersed across the surface of the catalyst and the reason for the highest concentration of metallic sites and H_2 consumption that was identified by CO-TPD and H_2-TPR, respectively. Blocking of pores has also been reported in the literature to adversely impact catalyst activity in the same way that was observed with lanthanum promotion which resulted in considerably lower reaction rates and TOF for every reaction compared to the other tested catalysts [98, 99 ,100].

Incorporation of niobium to the nickel catalyst demonstrated rather opposing results. Although k_1 was approximately half relative to 5Ni with 30.8 min^{-1}, dehydration reactions k_2 and k_6 radically increased to 58.0 min^{-1} and 67.4 min^{-1}, respectively, and consequentially made k_1 the rate-limiting step in the reaction. This was also reflected in the calculated TOF where k_2 increased significantly to 11.38 min^{-1} and k_6 to 13.92 min^{-1}, the highest of the three tested catalyst. This significant decrease in k_1 does not correlate with the total concentration of Ni metallic sites which was determined by CO-TPD to be relatively equal between 5Ni and 5Ni10Nb catalysts with 160 µmol g^{-1} and 180 µmol g^{-1}, respectively. Although, if we consider H_2-TPR results regarding the reducibility of the catalysts, it is clear that 5Ni10Nb catalyst has considerably lower total hydrogen consumption with 0.153 mmol g^{-1} compared to the 0.230 mmol g^{-1} which was observed for the 5Ni catalyst. This correlates very well with the difference in k_1 reaction rates between the two catalysts. Furthermore, average Ni particle size was determined to be around 7 nm with niobium promotion relative to 11 nm for the unpromoted 5Ni catalyst. This likely hindered carbonyl adsorption of HMF in a similar manner as observed with the 5Ni10La catalyst, owing to the lower k_1 and TOF relative to the 5Ni catalyst. At only 185 °C, DMF was the main product with 54% selectivity and steadily

increased to 69% product selectivity at 230 °C. This is likely a consequence of the higher number of acid sites that the 5Ni10Nb catalyst provided (5 times higher relative to 5Ni and 5Ni10La) and their expected Brønsted nature. Several studies have reported the preferential role Brønsted acid sites have over Lewis acidity for the dehydration of glycerol and furfural alcohol due to the fact that Nb-OH bonds are highly polarized for easier cleavage of the C-O bond [73,74,101,102].

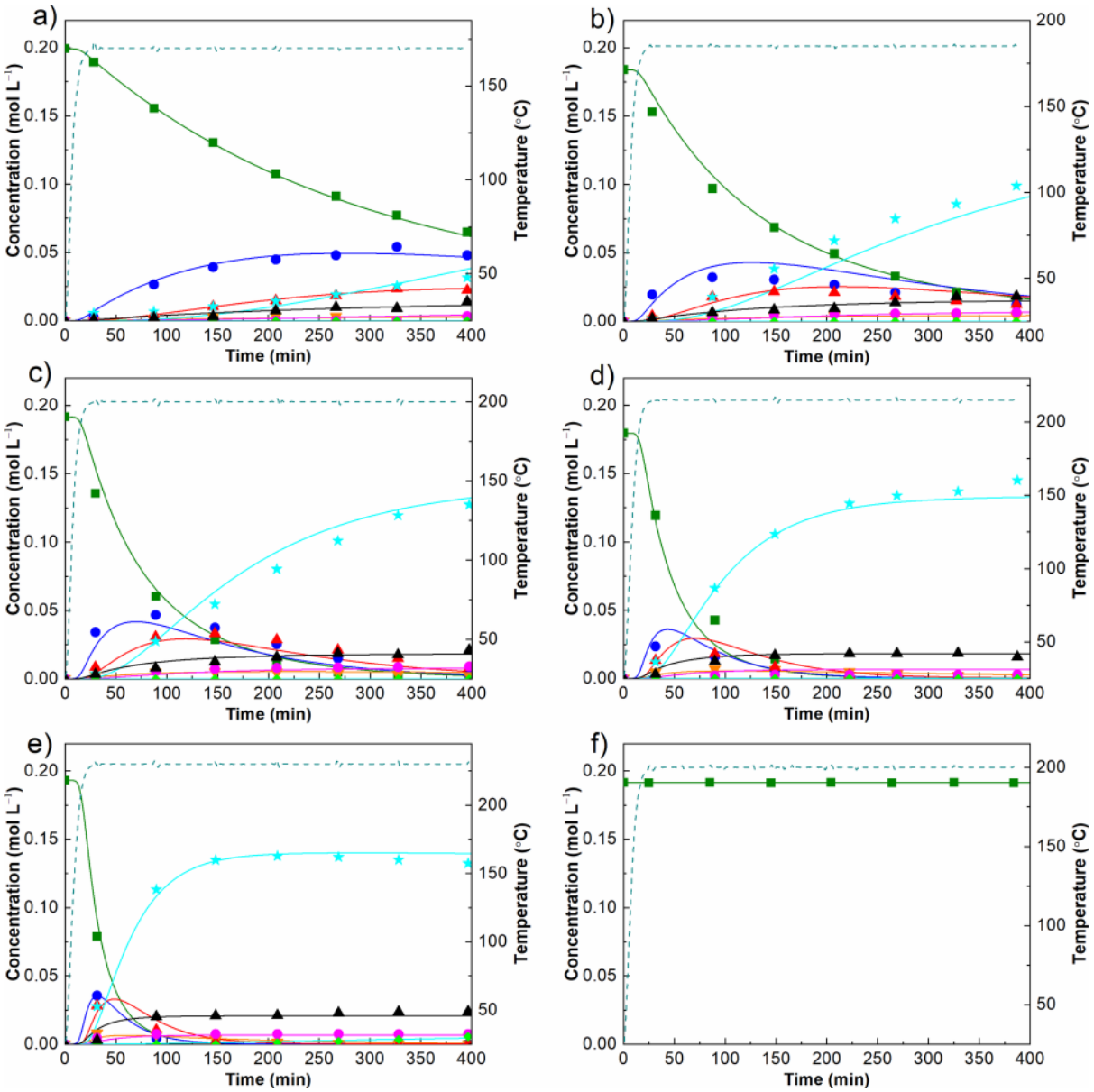

Figure 10. Temperature influence on product distribution over time using 5Ni10Nb/AC at a) 170 °C, b) 185 °C, c) 200 °C, d) 215 °C, e) 230 °C, and f) 10Nb at 200 °C. ■ HMF, ● BHMF, ▼ 5-MF, ▲ 2-HM-5-MF, ★ DMF, ● BHMTHF, ◆ DMTHF, ▲ Humins. - - - - Temperature. Model values correspond to lines, experimental values correspond with symbols.

The alternative reaction pathway via 5-MF remained insignificant, however, humin formation (k_8) increased modestly to 3.8 min^{-1} with an activation energy of only 107 kJ mol^{-1}, half that was observed with 5Ni. This correlates with reports specifically identifying the strong acidity associated with niobium to attribute to acid-catalyzed formation of humins and has even been observed to occur as low as 120 °C during dehydration of glucose [103–105]. Carbon balances considering only liquid phase products varied between catalysts; >85% for 5Ni, >96% for 5Ni10La, and as low as 75% for 5Ni10Nb. Thermal gravimetric analysis (TGA) was conducted (RuboTherm TG with dynamic GDS) on ~10 mg sample of spent 5Ni10Nb catalyst (used at 230 °C) in both air and nitrogen environments up to 700 °C. Fresh activated carbon support was also tested under air in the attempt to distinguish the contribution from formed coke and support as shown in Figure S.2. As observed in Figure S.2, the blank carbon support decomposed completely by approximately 600 °C in an oxygen-containing environment. We observed a similar trend when the spent 5Ni10Nb catalyst was subjected to the same TGA conditions in which a sudden loss in mass occurred between 525 °C and 600 °C which we contributed to the degradation of the carbon support. We also performed TGA in a nitrogen atmosphere with the spent catalyst to indicate the mass loss associated with desorption of water and other liquid products that were strongly adsorbed to the surface of the catalyst. Therefore, we associated the mass loss that occurred between 300 °C and 500 °C to be attributed to soft coke deposits, although this is an approximation. This temperature range is in good agreement with other studies which have attributed this mass loss to correspond to soft coke deposits on the catalyst [101,102,103,104]. It is expected that this spent catalyst would contain the maximum amount of carbonaceous depositions out of all activity tests performed as coke is known to be more readily formed in the presence of acid sites and at higher temperatures [110]. By extrapolating these results to the total amount of catalyst originally introduced prior to

activity tests, even with generous approximations, coke was determined to only contribute roughly 4% to the missing carbon balance. Finally, size-exclusion chromatography (SEC) was performed, where larger compounds above the molecular weight of HMF ranging between 200 Da up to 2000 Da were identified to be present in the liquid phase, shown in Figure S.4. Higher content was seen for tests conducted with niobium catalysts, although could not be quantified preciously. This confirms the presence of humins in the liquid phase and clarifies where the missing carbon balance equated from.

Interestingly, ring saturation of DMF to yield DMTHF (k_7) began to emerge at 230 °C but was not detected for the other catalysts under the same reaction conditions, contrary to the diminished reducibility observed during H_2-TPR (Table 2). This is possibly due to a combination of factors including reducing steric hindrance following removal of both alcohols, the presence of Brønsted acidity to allow adsorbance of the C=C bonds amongst the furan ring, and then finally the harsh reaction conditions to overcome the high energy barrier of 405 kJ mol^{-1} [111,112].

Table 4. Calculated kinetic parameters and TOF for HMF hydrotreatment over Ni-based catalysts.

Reaction rate constants at 200 °C (k_i), min^{-1}				Activation energies (Ea_i), kJ mol^{-1}			Turnover Frequencies at 230 °C (TOF), min^{-1}		
i	5Ni	5Ni10La	5Ni10Nb	5Ni	5Ni10La	5Ni10Nb	5Ni	5Ni10La	5Ni10Nb
1	61±2	7.5±0.2	30.8±0.9	100±2	83±2	95±3	12.94	1.75	6.93
2	23.3±1.5	0.90±0.05	58±4	164±7	97±6	103±6	4.56	0.21	11.38
3	<0.1	<0.1	1.4±0.5	120±40	130±90	127±40	0.01	0.01	0.31
4	0.3±0.3	0.2±0.2	3.7±0.7	140±50	140±90	142±60	0.06	0.06	0.88
5	3.3±0.5	0.53±0.06	3.3±0.8	108±17	25±13	94±23	0.09	0.11	0.64
6	37±3	0.9±0.2	67±5	140±36	27±20	77±8	7.23	0.20	13.92
7	<0.1	<0.1	0.4±0.1[a]	n.a.	n.a.	>300	0	0	0.10
8	1.4±0.2	<0.1	3.8±0.3	210±22	n.a.	107±9	0.29	0	0.86

[a] Reaction rate constant given for 230 °C.

3.5 Catalyst Recyclability and Stability

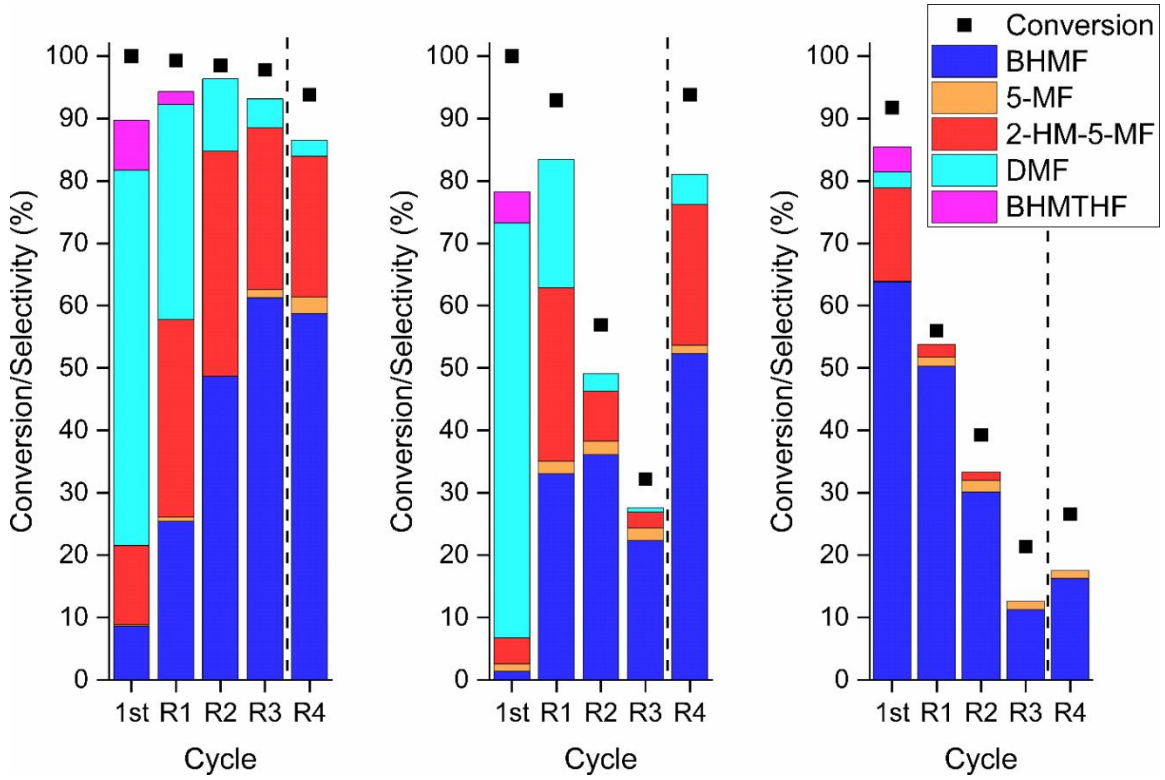

Figure 11. Recyclability tests of Ni (left), NiNb (middle), and NiLa (right) catalysts. Dashed line represents when regeneration of the catalyst was performed.

Recyclability tests of the carbon-supported catalysts with associated conversions and product selectivities are presented in Figure 11 where R1-4 represents the number of cycles. All carbon balances were determined to be >91% for all recycle tests and elemental analysis of the liquid products indicated no major Ni leaching (below 0.5 wt.% of starting Ni loading). Variations in catalyst activity and selectivity varied considerably between catalysts. 5Ni catalyst (left) demonstrated the smallest drop in conversion from 100% in the first test to 94% after the fourth recycle test. Product selectivity was significantly impacted, specifically impeding complete dehydration towards DMF where selectivity dropped from 60% in the initial activity test to only 3% after the final recycle test. Saturation of the furan ring to form BHMTHF was also undetectable following the first recycled test. Regeneration attempts via calcination had no favourable effect on restoring either activity or dehydration reactivity. Niobium and lanthanum promoted catalysts were much more significantly impacted during

recyclability tests. 5Ni10Nb catalyst (middle) demonstrated a substantial decrease in conversion from 100% in the initial test to as low as 32% during the third recycle. Likewise to the 5Ni catalyst, dehydration reactions were also considerably hindered as DMF selectivity plunged from 66% to 1% from the first test to the third recycled test, respectively. Interestingly, calcination in air restored activity of the niobium-containing catalyst to 94% conversion in the fourth recycle test, in proximity to its former original test. This return of activity following regeneration strongly implies that soft coke deposits were responsible for the decline in activity which were also observed to be present during TGA analysis of spent 5Ni10Nb (Figure S.2). In terms of selectivity, the first dehydration reaction to 2-HM-5-MF was renewed to 23%, but similarly to 5Ni catalyst, complete dehydration to DMF was not renewed to its prior selectivity. 5Ni10La catalyst underwent the most severe deactivation during recycling tests with HMF conversion falling from 92% in the first activity test to 21% in the third recycle test. Dehydration reactions were relatively nonexistent after the first activity test. Contrary to the niobium-promoted catalyst, regeneration of the 5Ni10La catalyst via calcination in air resulted in negligible improvements in activity. Following the fourth recycle test, the 5Ni10La catalyst was washed in THF and calcined once again under the same conditions as prior to remove any potential coke deposits before being subjected to H_2-TPR. The H_2 – TPR profile demonstrates a major double peak between 550 °C and 800 °C which was not present in the initial H_2-TPR profile prior to activity tests (Figure S.11). Literature has commonly shown this to be associated with perovskite-like structure of lanthanum nickelates (such as $LaNiO_3$) which require reduction temperatures above 400 °C to achieve complete reduction to metallic Ni [113] [114] [115]. The repetitive reduction and subsequent calcination of the 5Ni10La catalyst at elevated temperatures likely formed increasing amounts of irreducible (at least under our conditions) mixed oxides of Ni and La,

owing to its consistent deactivation throughout the recyclability tests, although this could not be precisely confirmed from XRD analysis.

It is difficult to explain the reasoning behind the consistent drop in dehydration reactions during the cumulative recyclability tests. SEM images of recycled catalysts (Figure S.8) do not indicate any obvious morphological alterations to the surface of the catalysts. Additionally, the variation of average particle diameter obtained from TEM lies in close proximity to the standard deviation with negligible differences between reduced, spent, and recycled catalysts suggesting no substantial nickel particle agglomerations or coarsening occurred (Figure S.10). Active sites necessary for dehydration reactions are anticipated to be negatively influenced or blocked by types of coke that could not be removed with a calcination temperature of 400 °C as has been similarly reported in Ni-containing catalysts, however, this could not be distinguished from the carbon support during TGA analysis [116] [117] [118].

4. Conclusion

This work prepared promoted nickel-based catalysts supported on activated carbon and tested their catalytic activity towards hydrodeoxygenation of 5-hydroxymethylfurfural to value-added products. Catalytic testing was conducted at 5 MPa of hydrogen over a range of reaction temperatures between 170 °C and 230 °C, offering a kinetic and mechanistic approach to HDO of HMF. Product distribution varied considerably between catalysts and was greatly influenced by reaction temperature. At reaction temperatures below 200 °C, 5Ni catalyst resulted in BHMF as the major product whereas deoxygenation products of 2-HM-5-MF and DMF formed at higher temperatures due to having to overcome higher activation energies. Lanthanum addition slowed all reaction rates and activity relative to non-promoted nickel, particularly dehydration reactions k_2 and k_6, thus significantly restricting product

selectivity to mainly BHMF despite the enhancement to reducibility. Conversely, incorporation of niobium accelerated dehydration reactions, enabling DMF to form at lower temperatures and predominately higher selectivity relative to only nickel. A microkinetic model is presented based on the proposed reaction pathway that considers adsorption and desorption kinetics onto active metallic sites, mass transfer between gas-liquid phases, and thermodynamic influences. Modelled values fit experimental results adequately well, providing insights into complex reaction mechanisms and catalyst design for efficient hydrodeoxygenation of bio-based compounds. Future work will expand on this microkinetic model by considering the participation of more than one active site, in addition to extended mass-transfer and adsorption kinetic phenomena.

Acknowledgements

The authors would like to appreciatively acknowledge the financial support of by the EU Framework Program for Research and Innovation Horizon 2020 under Grant agreement no. 814416 (Reaxpro) and the ARRS (Program P2-0152 and postdoctoral research project Z2-9200). Mr. Jošt Mohorko and his good friend Vili Resnik are acknowledged for their swift elemental analysis.

References

[1] G.W. Huber, S. Iborra, A. Corma, Synthesis of transportation fuels from biomass: Chemistry, catalysts, and engineering, Chem. Rev. 106 (2006) 4044–4098. https://doi.org/10.1021/cr068360d.

[2] F.H. Isikgor, C.R. Becer, Lignocellulosic biomass: a sustainable platform for the production of bio-based chemicals and polymers, Polym. Chem. 6 (2015) 4497–4559. https://doi.org/10.1039/c5py00263j.

[3] K. Kohli, R. Prajapati, B.K. Sharma, Bio-based chemicals from renewable biomass for integrated biorefineries, Energies. 12 (2019). https://doi.org/10.3390/en12020233.

[4] K.I. Galkin, V.P. Ananikov, When Will 5-Hydroxymethylfurfural, the "Sleeping Giant" of Sustainable Chemistry, Awaken?, ChemSusChem. (2019) 1–8. https://doi.org/10.1002/cssc.201900592.

[5] K. Dong, J. Zhang, W. Luo, L. Su, Z. Huang, Catalytic conversion of carbohydrates into 5-hydroxymethyl furfural over sulfonated hyper-cross-linked polymer in DMSO, Chem. Eng. J. 334 (2018) 1055–1064. https://doi.org/10.1016/j.cej.2017.10.092.

[6] F.K. Kazi, A.D. Patel, J.C. Serrano-Ruiz, J.A. Dumesic, R.P. Anex, Techno-economic analysis of dimethylfuran (DMF) and hydroxymethylfurfural (HMF) production from pure fructose in catalytic processes, Chem. Eng. J. 169 (2011) 329–338. https://doi.org/10.1016/j.cej.2011.03.018.

[7] H. Xu, C. Wang, A comprehensive review of 2,5-dimethylfuran as a biofuel candidate, Biofuels from Lignocellul. Biomass Innov. beyond Bioethanol. (2015) 105–129. https://doi.org/10.1002/9783527685318.ch5.

[8] Y. Román-Leshkov, C.J. Barrett, Z.Y. Liu, J.A. Dumesic, Production of dimethylfuran for liquid fuels from biomass-derived carbohydrates, Nature. 447 (2007) 982–985. https://doi.org/10.1038/nature05923.

[9] H. Cai, C. Li, A. Wang, T. Zhang, Biomass into chemicals: One-pot production of furan-based diols from carbohydrates via tandem reactions, Catal. Today. 234 (2014) 59–65. https://doi.org/10.1016/j.cattod.2014.02.029.

[10] C. Moreau, M.N. Belgacem, A. Gandini, Recent catalytic advances in the chemistry of substituted furans from carbohydrates and in the ensuing polymers, Top. Catal. 27 (2004) 11–30. https://doi.org/10.1023/B:TOCA.0000013537.13540.0e.

[11] Z. Si, X. Zhang, C. Wang, L. Ma, R. Dong, An Overview on Catalytic Hydrodeoxygenation of Pyrolysis Oil and Its Model Compounds, Catalysts. 7 (2017) 169. https://doi.org/10.3390/catal7060169.

[12] Z. He, X. Wang, Hydrodeoxygenation of model compounds and catalytic systems for pyrolysis bio-oils upgrading, Catal. Sustain. Energy. 1 (2013) 28–52. https://doi.org/10.2478/cse-2012-0004.

[13] W. Jin, L. Pastor-Pérez, J.J. Villora-Picó, A. Sepúlveda-Escribano, S. Gu, T.R. Reina, Investigating New Routes for Biomass Upgrading: "h2-Free" Hydrodeoxygenation Using Ni-Based Catalysts, ACS Sustain. Chem. Eng. 7 (2019) 16041–16049. https://doi.org/10.1021/acssuschemeng.9b02712.

[14] X. Kong, R. Zheng, Y. Zhu, G. Ding, Y. Zhu, Y.W. Li, Rational design of Ni-based catalysts derived from hydrotalcite for selective hydrogenation of 5-hydroxymethylfurfural, Green Chem. 17 (2015) 2504–2514. https://doi.org/10.1039/c5gc00062a.

[15] P. Gallezot, P.J. Cerino, B. Blanc, G. Flèche, P. Fuertes, Glucose hydrogenation on promoted raney-nickel catalysts, J. Catal. 146 (1994) 93–102. https://doi.org/10.1016/0021-9517(94)90012-4.

[16] P.M. Mortensen, J.D. Grunwaldt, P.A. Jensen, A.D. Jensen, Screening of catalysts for hydrodeoxygenation of phenol as a model compound for bio-oil, ACS Catal. 3 (2013) 1774–1785. https://doi.org/10.1021/cs400266e.

[17] B. Pomeroy, T. Doxtator, J.E. Herrera, D. Pjontek, Effect of Ni reducibility on anisole hydrodeoxygenation activity in the La-Ni/γ-Al2O3 Catalytic System, Int. J. Chem. React. Eng. 18 (2020). https://doi.org/10.1515/ijcre-2019-0066.

[18] D.S. Costa, R.S. Gomes, C.B. Rodella, R.B. da Silva, R. Fréty, É. Teixeira Neto, S.T. Brandão, Study of nickel, lanthanum and niobium-based catalysts applied in the partial oxidation of methane, Catal. Today. (2018) 1–9. https://doi.org/10.1016/j.cattod.2018.10.022.

[19] J. Lu, X. Li, S. He, C. Han, G. Wan, Y. Lei, R. Chen, P. Liu, K. Chen, L. Zhang, Y. Luo, Hydrogen production via methanol steam reforming over Ni-based catalysts: Influences of Lanthanum (La) addition and supports, Int. J. Hydrogen Energy. 42 (2017) 3647–3657. https://doi.org/10.1016/j.ijhydene.2016.08.165.

[20] J. Huang, R. Ma, T. Huang, A. Zhang, W. Huang, Carbon dioxide reforming of methane over Ni/Mo/SBA-15-La 2 O 3 catalyst: Its characterization and catalytic performance, J. Nat. Gas Chem. 20 (2011) 465–470. https://doi.org/10.1016/S1003-9953(10)60226-5.

[21] A.N. Fatsikostas, D.I. Kondarides, X.E. Verykios, Production of hydrogen for fuel cells by reformation of biomass-derived ethanol, Catal. Today. 75 (2002) 145–155. https://doi.org/10.1016/S0920-5861(02)00057-3.

[22] Q.L.M. Ha, U. Armbruster, C. Kreyenschulte, H. Atia, H. Lund, H.T. Vuong, S. Wohlrab, Stabilization of low nickel content catalysts with lanthanum and by citric acid assisted preparation to suppress deactivation in dry reforming of methane, Catal. Today. 334 (2019) 203–214. https://doi.org/10.1016/j.cattod.2018.11.021.

[23] B. Savova, S. Loridant, D. Filkova, J.M.M. Millet, Ni-Nb-O catalysts for ethane oxidative dehydrogenation, Appl. Catal. A Gen. 390 (2010) 148–157. https://doi.org/10.1016/j.apcata.2010.10.004.

[24] C. Hernández Mejía, C. Vogt, B.M. Weckhuysen, K.P. de Jong, Stable niobia-supported nickel catalysts for the hydrogenation of carbon monoxide to hydrocarbons, Catal. Today. (2018) 0–1. https://doi.org/10.1016/j.cattod.2018.11.036.

[25] A.A.A. da Silva, N. Bion, F. Epron, S. Baraka, F.C. Fonseca, R.C. Rabelo-Neto, L. V. Mattos, F.B. Noronha, Effect of the type of ceria dopant on the performance of Ni/CeO2 SOFC anode for ethanol internal reforming, Appl. Catal. B Environ. 206 (2017) 626–641. https://doi.org/10.1016/j.apcatb.2017.01.069.

[26] E. Bailón-García, F.J. Maldonado-Hódar, A.F. Pérez-Cadenas, F. Carrasco-Marín, Catalysts supported on carbon materials for the selective hydrogenation of citral, Catalysts. 3 (2013) 853–877. https://doi.org/10.3390/catal3040853.

[27] M.A. Álvarez-Montero, J.J. Rodriguez, L.M. Gómez-Sainero, Platinum nanoparticles supported on activated carbon catalysts for the gasphase hydrodechlorination of dichloromethane: Influence of catalyst composition and operating conditions, Nanomater. Nanotechnol. 6 (2016). https://doi.org/10.5772/62593.

[28] D.M. Alonso, S.G. Wettstein, J.A. Dumesic, D.M. Alonso, G. Wettstein, J.A. Dumesic, Chem Soc Rev Bimetallic catalysts for upgrading of biomass to fuels and chemicals w, 41 (2012). https://doi.org/10.1039/c2cs35188a.

[29] S. Nishimura, N. Ikeda, K. Ebitani, Selective hydrogenation of biomass-derived 5-hydroxymethylfurfural (HMF) to 2,5-dimethylfuran (DMF) under atmospheric hydrogen pressure over carbon supported PdAu bimetallic catalyst, Catal. Today. 232 (2014) 89–98. https://doi.org/10.1016/j.cattod.2013.10.012.

[30] L. Yu, L. He, J. Chen, J. Zheng, L. Ye, H. Lin, Y. Yuan, Robust and recyclable nonprecious bimetallic nanoparticles on carbon nanotubes for the hydrogenation and hydrogenolysis of 5-hydroxymethylfurfural, ChemCatChem. 7 (2015) 1701–1707. https://doi.org/10.1002/cctc.201500097.

[31] J. Gu, J. Zhang, Y. Wang, D. Li, H. Huang, H. Yuan, Y. Chen, Efficient transfer hydrogenation of biomass derived furfural and levulinic acid via magnetic zirconium nanoparticles: Experimental and kinetic study, Ind. Crops Prod. 145 (2020) 112133. https://doi.org/10.1016/j.indcrop.2020.112133.

[32] J. Zhang, J. Chen, Selective Transfer Hydrogenation of Biomass-Based Furfural and 5-Hydroxymethylfurfural over Hydrotalcite-Derived Copper Catalysts Using Methanol as a Hydrogen Donor, ACS Sustain. Chem. Eng. 5 (2017) 5982–5993. https://doi.org/10.1021/acssuschemeng.7b00778.

[33] L. Penín, S. Peleteiro, R. Yáñez, J.C. Parajó, V. Santos, Kinetics of 5-Hydroxymethylfurfural production from monosaccharides in media containing an ionic liquid and a solid acid catalyst, BioResources. 12 (2017) 8402–8418. https://doi.org/10.15376/biores.12.4.8402-8418.

[34] D. Jung, P. Körner, A. Kruse, Kinetic study on the impact of acidity and acid concentration on the formation of 5-hydroxymethylfurfural (HMF), humins, and levulinic acid in the hydrothermal conversion of fructose, Biomass Convers. Biorefinery. (2019). https://doi.org/10.1007/s13399-019-00507-0.

[35] N. Nikbin, S. Caratzoulas, D.G. Vlachos, A first principles-based microkinetic model for the conversion of fructose to 5-hydroxymethylfurfural, ChemCatChem. 4 (2012) 504–511. https://doi.org/10.1002/cctc.201100444.

[36] M.S. Gyngazova, L. Negahdar, L.C. Blumenthal, R. Palkovits, Experimental and kinetic analysis of the liquid phase hydrodeoxygenation of 5-hydroxymethylfurfural to 2,5-dimethylfuran over carbon-supported nickel catalysts, Chem. Eng. Sci. 173 (2017) 455–464. https://doi.org/10.1016/j.ces.2017.07.045.

[37] J.N.M. Tan-Soetedjo, H.H. Van De Bovenkamp, R.M. Abdilla, C.B. Rasrendra, J. Van Ginkel, H.J. Heeres, Experimental and Kinetic Modeling Studies on the Conversion of Sucrose to Levulinic Acid and 5-Hydroxymethylfurfural Using Sulfuric Acid in Water, Ind. Eng. Chem. Res. 56 (2017) 13228–13239. https://doi.org/10.1021/acs.iecr.7b01611.

[38] M.C. Sánchez-Sánchez, R.M. Navarro, J.L.G. Fierro, Ethanol steam reforming over Ni/La-Al2O3 catalysts: Influence of lanthanum loading, Catal. Today. 129 (2007) 336–345. https://doi.org/10.1016/j.cattod.2006.10.013.

[39] I.E. Wachs, Y. Chen, J.M. Jehng, L.E. Briand, T. Tanaka, Molecular structure and reactivity of the Group V metal oxides, Catal. Today. 78 (2003) 13–24. https://doi.org/10.1016/S0920-5861(02)00337-1.

[40] I. Nowak, M. Ziolek, Niobium Compounds: Preparation, Characterization, and Application in Heterogeneous Catalysis, Chem. Rev. 99 (1999) 3603–3624. https://doi.org/10.1021/cr9800208.

[41] P. Munnik, P.E. De Jongh, K.P. De Jong, Recent Developments in the Synthesis of Supported Catalysts, Chem. Rev. 115 (2015) 6687–6718. https://doi.org/10.1021/cr500486u.

[42] N.M. Deraz, The comparative jurisprudence of catalysts preparation methods: I. precipitation

and impregnation methods, J. Ind. Environ. Chem. 2 (2018) 19–21.

[43] Z. Cheng, J.L. Everhart, G. Tsilomelekis, V. Nikolakis, B. Saha, D.G. Vlachos, Structural analysis of humins formed in the Brønsted acid catalyzed dehydration of fructose, Green Chem. 20 (2018) 997–1006. https://doi.org/10.1039/c7gc03054a.

[44] H. Wang, H. Da, R. Wang, S. Ji, Beef-derived mesoporous carbon as highly efficient support for PtRuIr electrocatalysts and their high activity for CO and methanol oxidation, South African J. Chem. 67 (2014) 33–39.

[45] M. Carmo, M. Linardi, J.G.R. Poco, H2O2 treated carbon black as electrocatalyst support for polymer electrolyte membrane fuel cell applications, Int. J. Hydrogen Energy. 33 (2008) 6289–6297. https://doi.org/10.1016/j.ijhydene.2008.08.021.

[46] H. Wang, H. Da, S. Ji, S. Liao, R. Wang, Selenium-Functionalized Carbon as a Support for Platinum Nanoparticles with Improved Electrochemical Properties for the Oxygen Reduction Reaction and CO Tolerance, J. Electrochem. Soc. 160 (2013) H266–H270. https://doi.org/10.1149/2.014306jes.

[47] M. Carmo, A.R. dos Santos, J.G.R. Poco, M. Linardi, Physical and electrochemical evaluation of commercial carbon black as electrocatalysts supports for DMFC applications, J. Power Sources. 173 (2007) 860–866. https://doi.org/10.1016/j.jpowsour.2007.08.032.

[48] J.F. Moulder, W.F. Stickle, P.E. Sobol, K.D. Bomben, Handbook of X-Ray Photoelectron Spectroscopy, 1995. https://doi.org/10.1002/0470014229.ch22.

[49] S. Mickevičius, S. Grebinskij, V. Bondarenka, B. Vengalis, K. Šliužiene, B.A. Orlowski, V. Osinniy, W. Drube, Investigation of epitaxial LaNiO3-x thin films by high-energy XPS, J. Alloys Compd. 423 (2006) 107–111. https://doi.org/10.1016/j.jallcom.2005.12.038.

[50] J. Sehested, J.A.P. Gelten, S. Helveg, Sintering of nickel catalysts: Effects of time, atmosphere, temperature, nickel-carrier interactions, and dopants, Appl. Catal. A Gen. 309 (2006) 237–246. https://doi.org/10.1016/j.apcata.2006.05.017.

[51] X. Li, L. Feng, L. Zhang, D.B. Dadyburjor, E.L. Kugler, Alcohol synthesis over pre-reduced activated carbon-supported molybdenum-based catalysts, Molecules. 8 (2003) 13–30. https://doi.org/10.3390/80100013.

[52] Z. Zhang, X.E. Verykios, Carbon dioxide reforming of methane to synthesis gas over Ni/La2O3 catalysts, Appl. Catal. A Gen. 138 (1996) 109–133. https://doi.org/10.1016/j.ijhydene.2011.01.034.

[53] J. Xu, W. Zhou, J. Wang, Z. Li, J. Ma, Characterization and analysis of carbon deposited during the dry reforming of methane over Ni/La2O3/Al2O3 catalysts, Cuihua Xuebao/Chinese J. Catal. 30 (2009) 1076–1084. https://doi.org/10.1016/s1872-2067(08)60139-4.

[54] J.R. Gavarri, B. Bakiz, F. Guinneton, M. Arab, A. Benlhachemi, S. Villain, P. Satre, Carbonatation and decarbonatation kinetics in the La2O 3-La2O2CO3 system under CO 2 gas flows, Adv. Mater. Sci. Eng. 2010 (2010) 0–7. https://doi.org/10.1155/2010/360597.

[55] F.P. Cardoso, A.E. Nogueira, P.S.O. Patrício, L.C.A. Oliveira, Effect of tungsten doping on catalytic properties of niobium oxide, J. Braz. Chem. Soc. 23 (2012) 702–709. https://doi.org/10.1590/s0103-50532012000400016.

[56] T.C. Ramalho, L.C.A. Oliveira, K.T.G. Carvalho, E.F. Souza, E.F.F. Da Cunha, M. Nazzaro, The molecular basis for the behaviour of niobia species in oxidation reaction probed by theoretical calculations and experimental techniques, Mol. Phys. 107 (2009) 171–179. https://doi.org/10.1080/00268970902769489.

[57] D.S. Costa, R.S. Gomes, C.B. Rodella, R.B. da Silva, R. Fréty, É. Teixeira Neto, S.T. Brandão,

Study of nickel, lanthanum and niobium-based catalysts applied in the partial oxidation of methane, Catal. Today. (2018) 1–9. https://doi.org/10.1016/j.cattod.2018.10.022.

[58] L.F. de Sousa, F.S. Toniolo, S.M. Landi, M. Schmal, Investigation of structures and metallic environment of the Ni/Nb2O5 by different in situ treatments – Effect on the partial oxidation of methane, Appl. Catal. A Gen. 537 (2017) 100–110. https://doi.org/10.1016/j.apcata.2017.03.015.

[59] K.V.R. Chary, K.S. Lakshmi, P.V.R. Rao, K.S.R. Rao, M. Papadaki, Characterization and catalytic properties of niobia supported nickel catalysts in the hydrodechlorination of 1,2,4-trichlorobenzene, J. Mol. Catal. A Chem. 223 (2004) 353–361. https://doi.org/10.1016/j.molcata.2003.09.049.

[60] K. V. Manukyan, A.G. Avetisyan, C.E. Shuck, H.A. Chatilyan, S. Rouvimov, S.L. Kharatyan, A.S. Mukasyan, Nickel Oxide Reduction by Hydrogen: Kinetics and Structural Transformations, J. Phys. Chem. C. 119 (2015) 16131–16138. https://doi.org/10.1021/acs.jpcc.5b04313.

[61] Z. Zhang, Z. Chen, H. Chen, X. Gou, K. Chen, X. Lu, P. Ouyang, J. Fu, Catalytic decarbonylation of stearic acid to hydrocarbons over activated carbon-supported nickel, Sustain. Energy Fuels. 2 (2018) 1837–1843. https://doi.org/10.1039/c8se00189h.

[62] M.C. Le, K. Le Van, T.H.T. Nguyen, N.H. Nguyen, The Impact of Ce-Zr Addition on Nickel Dispersion and Catalytic Behavior for CO2 Methanation of Ni/AC Catalyst at Low Temperature, J. Chem. 2017 (2017). https://doi.org/10.1155/2017/4361056.

[63] L.M. Cam, N.T.T. Ha, L. Van Khu, N.N. Ha, T.C. Brown, Carbon Dioxide Methanation over Nickel Catalysts Supported on Activated Carbon at Low Temperature, Aust. J. Chem. (2019). https://doi.org/10.1071/CH19355.

[64] L. Huang, Y. Lv, S. Wu, P. Liu, W. Xiong, F. Hao, H. Luo, Activated carbon supported bimetallic catalysts with combined catalytic effects for aromatic nitro compounds hydrogenation under mild conditions, Appl. Catal. A Gen. 577 (2019) 76–85. https://doi.org/10.1016/j.apcata.2019.03.017.

[65] P. Rodríguez-Estupiñán, L. Giraldo, J. Moreno-Piraján, Nickel(II) ion adsorption onto activated carbon. Relationship between physicochemical properties and adsorption capacity, Adsorpt. Sci. Technol. 29 (2011) 541–551. https://doi.org/10.1260/0263-6174.29.6.541.

[66] Q. Jeangros, T.W. Hansen, J.B. Wagner, C.D. Damsgaard, R.E. Dunin-Borkowski, C. Hébert, J. Van Herle, A. Hessler-Wyser, Reduction of nickel oxide particles by hydrogen studied in an environmental TEM, J. Mater. Sci. 48 (2013) 2893–2907. https://doi.org/10.1007/s10853-012-7001-2.

[67] A.S. Al-Fatesh, M.A. Naeem, A.H. Fakeeha, A.E. Abasaeed, Role of La2O3 as promoter and support in Ni/??-Al2O3 catalysts for dry reforming of methane, Chinese J. Chem. Eng. 22 (2014) 28–37. https://doi.org/10.1016/S1004-9541(14)60029-X.

[68] E. Heracleous, A.A. Lemonidou, Ni-Nb-O mixed oxides as highly active and selective catalysts for ethene production via ethane oxidative dehydrogenation. Part I: Characterization and catalytic performance, J. Catal. 237 (2006) 162–174. https://doi.org/10.1016/j.jcat.2005.11.002.

[69] J. He, M.R. Nielsen, T.W. Hansen, S. Yang, A. Riisager, Hierarchically constructed NiO with improved performance for catalytic transfer hydrogenation of biomass-derived aldehydes, Catal. Sci. Technol. 9 (2019) 1289–1300. https://doi.org/10.1039/c8cy02536c.

[70] M. Li, J. Fu, S. Xing, L. Yang, X. Zhang, P. Lv, Z. Wang, Z. Yuan, A novel catalyst with variable active sites for the direct hydrogenation of waste oils into jet fuel, Appl. Catal. B

Environ. 260 (2020) 118114. https://doi.org/10.1016/j.apcatb.2019.118114.

[71] M.A. Sanhoob, O. Muraza, M. Yoshioka, M. Qamaruddin, T. Yokoi, Lanthanum, cerium, and boron incorporated ZSM-12 zeolites for catalytic cracking of n-hexane, J. Anal. Appl. Pyrolysis. 129 (2018) 231–240. https://doi.org/10.1016/j.jaap.2017.11.007.

[72] C.D. Evans, S.A. Kondrat, P.J. Smith, T.D. Manning, P.J. Miedziak, G.L. Brett, R.D. Armstrong, J.K. Bartley, S.H. Taylor, M.J. Rosseinsky, G.J. Hutchings, The preparation of large surface area lanthanum based perovskite supports for AuPt nanoparticles: Tuning the glycerol oxidation reaction pathway by switching the perovskite B site, Faraday Discuss. 188 (2016) 427–450. https://doi.org/10.1039/c5fd00187k.

[73] J.M. Jehng, I.E. Wachs, Molecular structures of supported niobium oxide catalysts under in situ conditions, J. Phys. Chem. 95 (1991) 7373–7379. https://doi.org/10.1021/j100172a049.

[74] X. Chan, T. Pu, X. Chen, A. James, J. Lee, J.B. Parise, D.H. Kim, T. Kim, Effect of niobium oxide phase on the furfuryl alcohol dehydration, Catal. Commun. 97 (2017) 65–69. https://doi.org/10.1016/j.catcom.2017.04.019.

[75] T.W. van Deelen, C. Hernández Mejía, K.P. de Jong, Control of metal-support interactions in heterogeneous catalysts to enhance activity and selectivity, Nat. Catal. 2 (2019) 955–970. https://doi.org/10.1038/s41929-019-0364-x.

[76] X. Xiao, H. Bergstrom, R. Saenger, B. Johnson, R. Sun, A. Peterson, The role of oxygen vacancies in biomass deoxygenation by reducible zinc/zinc oxide catalysts, Catal. Sci. Technol. 8 (2018) 1819–1827. https://doi.org/10.1039/c7cy02535a.

[77] E. Brunner, Solubility of Hydrogen in 10 Organic Solvents at 298.15, 323.15, and 373.15 K, J. Chem. Eng. Data. 30 (1985) 269–273. https://doi.org/10.1021/je00041a010.

[78] I. van Zandvoort, Towards the Valorization of Humin By-products : Characterization , Solubilization and Catalysis, 2015. https://doi.org/10.1111/j.1365-2426.2003.01178.x.

[79] M. Grilc, B. Likozar, Levulinic acid hydrodeoxygenation, decarboxylation and oligmerization over NiMo/Al2O3 catalyst to bio-based value-added chemicals: Modelling of mass transfer, thermodynamics and micro-kinetics, Chem. Eng. J. 330 (2017) 383–397. https://doi.org/10.1016/j.cej.2017.07.145.

[80] Y.B. Huang, M.Y. Chen, L. Yan, Q.X. Guo, Y. Fu, Nickel-tungsten carbide catalysts for the production of 2,5-dimethylfuran from biomass-derived molecules, ChemSusChem. 7 (2014) 1068–1072. https://doi.org/10.1002/cssc.201301356.

[81] D. Shi, R. Wojcieszak, S. Paul, E. Marceau, Ni promotion by fe: What benefits for catalytic hydrogenation?, Catalysts. 9 (2019). https://doi.org/10.3390/catal9050451.

[82] Rodiansono, S. Khairi, T. Hara, N. Ichikuni, S. Shimazu, Highly efficient and selective hydrogenation of unsaturated carbonyl compounds using Ni-Sn alloy catalysts, Catal. Sci. Technol. 2 (2012) 2139–2145. https://doi.org/10.1039/c2cy20216f.

[83] X. Cui, H. Yuan, K. Junge, C. Topf, M. Beller, F. Shi, A stable and practical nickel catalyst for the hydrogenolysis of C-O bonds, Green Chem. 19 (2017) 305–310. https://doi.org/10.1039/c6gc01955b.

[84] J. Long, Y. Xu, W. Zhao, H. Li, S. Yang, Heterogeneous Catalytic Upgrading of Biofuranic Aldehydes to Alcohols, Front. Chem. 7 (2019). https://doi.org/10.3389/fchem.2019.00529.

[85] J. Chen, R. Liu, Y. Guo, L. Chen, H. Gao, Selective hydrogenation of biomass-based 5-hydroxymethylfurfural over catalyst of palladium immobilized on amine-functionalized metal-organic frameworks, ACS Catal. 5 (2015) 722–733. https://doi.org/10.1021/cs5012926.

[86] D. A., S. D., Methods and Applications of Deoxygenation for the Conversion of Biomass to

Petrochemical Products, Biomass Now - Cultiv. Util. (2013). https://doi.org/10.5772/53983.

[87] B. Chen, Z. ming Shi, S. jian Jiang, H. Tian, Mechanism studies of 5-HMF pyrolysis by quantum chemistry, J. Cent. South Univ. 24 (2017) 2565–2571. https://doi.org/10.1007/s11771-017-3670-y.

[88] Y. Nakagawa, K. Takada, M. Tamura, K. Tomishige, Total hydrogenation of furfural and 5-hydroxymethylfurfural over supported Pd-Ir alloy catalyst, ACS Catal. 4 (2014) 2718–2726. https://doi.org/10.1021/cs500620b.

[89] S. Sitthisa, T. Sooknoi, Y. Ma, P.B. Balbuena, D.E. Resasco, Kinetics and mechanism of hydrogenation of furfural on Cu/SiO2 catalysts, J. Catal. 277 (2011) 1–13. https://doi.org/10.1016/j.jcat.2010.10.005.

[90] A. Saadi, R. Merabti, Z. Rassoul, M.M. Bettahar, Benzaldehyde hydrogenation over supported nickel catalysts, J. Mol. Catal. A Chem. 253 (2006) 79–85. https://doi.org/10.1016/j.molcata.2006.03.003.

[91] Y. Hou, Y. Wang, F. He, W. Mi, Z. Li, Z. Mi, W. Wu, E. Min, Effects of lanthanum addition on Ni-B/γ-Al2O3 amorphous alloy catalysts used in anthraquinone hydrogenation, Appl. Catal. A Gen. 259 (2004) 35–40. https://doi.org/10.1016/j.apcata.2003.09.006.

[92] H. Li, H. Li, J. Deng, Glucose hydrogenation over Ni-B/SiO2 amorphous alloy catalyst and the promoting effect of metal dopants, 74 (2002) 53–63.

[93] P. Mäki-Arvela, J. Hájek, T. Salmi, D.Y. Murzin, Chemoselective hydrogenation of carbonyl compounds over heterogeneous catalysts, Appl. Catal. A Gen. 292 (2005) 1–49. https://doi.org/10.1016/j.apcata.2005.05.045.

[94] M. Englisch, A. Jentys, J.A. Lercher, Structure sensitivity of the hydrogenation of crotonaldehyde over Pt/SiO2 and Pt/TiO2, J. Catal. 166 (1997) 25–35. https://doi.org/10.1006/jcat.1997.1494.

[95] V. V. Pushkarev, N. Musselwhite, K. An, S. Alayoglu, G.A. Somorjai, High structure sensitivity of vapor-phase furfural decarbonylation/ hydrogenation reaction network as a function of size and shape of Pt nanoparticles, Nano Lett. 12 (2012) 5196–5201. https://doi.org/10.1021/nl3023127.

[96] J. Wang, Y. Wang, G. Chen, Z. He, Highly loaded and dispersed Ni2P/Al2O3 catalyst with high selectivity for hydrogenation of acetophenone, Catalysts. 8 (2018). https://doi.org/10.3390/catal8080309.

[97] X. Kong, Y. Zhu, Z. Fang, J.A. Kozinski, I.S. Butler, L. Xu, H. Song, X. Wei, Catalytic conversion of 5-hydroxymethylfurfural to some value-added derivatives, Green Chem. 20 (2018) 3657–3682. https://doi.org/10.1039/c8gc00234g.

[98] M. Iwamoto, Y. Tanaka, N. Sawamura, S. Namba, Remarkable Effect of Pore Size on the Catalytic Activity of Mesoporous Silica for the Acetalization of Cyclohexanone with Methanol, J. Am. Chem. Soc. 125 (2003) 13032–13033. https://doi.org/10.1021/ja0375129.

[99] I.T. Ghampson, C. Newman, L. Kong, E. Pier, K.D. Hurley, R.A. Pollock, B.R. Walsh, B. Goundie, J. Wright, M.C. Wheeler, R.W. Meulenberg, W.J. Desisto, B.G. Frederick, R.N. Austin, Effects of pore diameter on particle size, phase, and turnover frequency in mesoporous silica supported cobalt Fischer-Tropsch catalysts, Appl. Catal. A Gen. 388 (2010) 57–67. https://doi.org/10.1016/j.apcata.2010.08.028.

[100] M.Y. Byun, D.W. Park, M.S. Lee, Effect of oxide supports on the activity of PD based catalysts for furfural hydrogenation, Catalysts. 10 (2020) 1–19. https://doi.org/10.3390/catal10080837.

[101] G.F. Leal, S. Lima, I. Graça, H. Carrer, D.H. Barrett, E. Teixeira-Neto, A.A.S. Curvelo, C.B. Rodella, R. Rinaldi, Design of Nickel Supported on Water-Tolerant Nb2O5 Catalysts for the Hydrotreating of Lignin Streams Obtained from Lignin-First Biorefining, IScience. 15 (2019) 467–488. https://doi.org/10.1016/j.isci.2019.05.007.

[102] G.S. Foo, D. Wei, D.S. Sholl, C. Sievers, Role of Lewis and brønsted acid sites in the dehydration of glycerol over niobia, ACS Catal. 4 (2014) 3180–3192. https://doi.org/10.1021/cs5006376.

[103] A. Jouve, S. Cattaneo, D. Delgado, N. Scotti, C. Evangelisti, J.M.L. Nieto, L. Prati, Furfural hydrogenation on modified niobia, Appl. Sci. 9 (2019). https://doi.org/10.3390/app9112287.

[104] P. Carniti, A. Gervasini, S. Biella, A. Auroux, Niobic acid and niobium phosphate as highly acidic viable catalysts in aqueous medium: Fructose dehydration reaction, Catal. Today. 118 (2006) 373–378. https://doi.org/10.1016/j.cattod.2006.07.024.

[105] K. Lourvanij, G.L. Rorrer, Reactions of Aqueous Glucose Solutions over Solid-Acid Y-Zeolite Catalyst at 110–160 °C, Ind. Eng. Chem. Res. 32 (1993) 11–19. https://doi.org/10.1021/ie00013a002.

[106] R. Prajapati, K. Kohli, S.K. Maity, Residue upgradation with slurry phase catalyst: Effect of feedstock properties, Fuel. 239 (2019) 452–460. https://doi.org/10.1016/j.fuel.2018.11.041.

[107] N.D. Charisiou, S.L. Douvartzides, G.I. Siakavelas, L. Tzounis, V. Sebastian, V. Stolojan, S.J. Hinder, M.A. Baker, K. Polychronopoulou, M.A. Goula, The relationship between reaction temperature and carbon deposition on nickel catalysts based on al2o3, zro2 or sio2 supports during the biogas dry reforming reaction, Catalysts. 9 (2019). https://doi.org/10.3390/catal9080676.

[108] N.D. Charisiou, K.N. Papageridis, L. Tzounis, V. Sebastian, S.J. Hinder, M.A. Baker, M. AlKetbi, K. Polychronopoulou, M.A. Goula, Ni supported on CaO-MgO-Al2O3 as a highly selective and stable catalyst for H2 production via the glycerol steam reforming reaction, Int. J. Hydrogen Energy. 44 (2019) 256–273. https://doi.org/10.1016/j.ijhydene.2018.02.165.

[109] H. Zhang, S. Shao, R. Xiao, D. Shen, J. Zeng, Characterization of coke deposition in the catalytic fast pyrolysis of biomass derivates, Energy and Fuels. 28 (2014) 52–57. https://doi.org/10.1021/ef401458y.

[110] M. Guisnet, P. Magnoux, Organic chemistry of coke formation, Appl. Catal. A Gen. 212 (2001) 83–96. https://doi.org/10.1016/S0926-860X(00)00845-0.

[111] T.S. Hansen, K. Barta, P.T. Anastas, P.C. Ford, A. Riisager, One-pot reduction of 5-hydroxymethylfurfural via hydrogen transfer from supercritical methanol, Green Chem. 14 (2012) 2457–2461. https://doi.org/10.1039/c2gc35667h.

[112] M. D'Ischia, A. Napolitano, A. Pezzella, Furans and their benzo derivatives: Applications, 2008. https://doi.org/10.1016/b978-008096518-5.00047-2.

[113] B.S. Barros, J. Kulesza, D.M. De Araújo Melo, A. Kiennemand, Nickel-based catalyst precursor prepared via microwave-induced combustion method: Thermodynamics of synthesis and performance in dry reforming of CH4, Mater. Res. 18 (2015) 732–739. https://doi.org/10.1590/1516-1439.018115.

[114] C. Alvarez-Galvan, M. Melian, L. Ruiz-Matas, J.L. Eslava, R.M. Navarro, M. Ahmadi, B.R. Cuenya, J.L.G. Fierro, Partial oxidation of methane to syngas over nickel-based catalysts: Influence of support type, addition of rhodium, and preparation method, Front. Chem. 7 (2019) 1–16. https://doi.org/10.3389/fchem.2019.00104.

[115] S. Kühl, H. Düdder, F. Girgsdies, K. Kähler, M. Muhler, M. Behrens, Perovskites as Precursors for Ni/La2O3 Catalysts in the Dry Reforming of Methane: Synthesis by Constant

pH Co-Precipitation, Reduction Mechanism and Effect of Ru-Doping, Zeitschrift Fur Anorg. Und Allg. Chemie. 643 (2017) 1088–1095. https://doi.org/10.1002/zaac.201700141.

[116] P. Lu, Q. Huang, A.C. Bourtsalas, Y. Chi, J. Yan, Effect of Operating Conditions on the Coke Formation and Nickel Catalyst Performance During Cracking of Tar, Waste and Biomass Valorization. 10 (2019) 155–165. https://doi.org/10.1007/s12649-017-0044-5.

[117] M.D. Zhurka, A.A. Lemonidou, J.A. Anderson, P.N. Kechagiopoulos, Kinetic analysis of the steam reforming of ethanol over Ni/SiO2 for the elucidation of metal-dominated reaction pathways, React. Chem. Eng. 3 (2018) 883–897. https://doi.org/10.1039/c8re00145f.

[118] C. Zhang, X. Hu, Z. Zhang, L. Zhang, D. Dong, G. Gao, R. Westerhof, S.S.A. Syed-Hassan, Steam reforming of acetic acid over Ni/Al2O3 catalyst: Correlation of calcination temperature with the interaction of nickel and alumina, Fuel. 227 (2018) 307–324. https://doi.org/10.1016/j.fuel.2018.04.111.

Figure captions

Figure 1. SEM images of carbon-supported 5Ni (a-b), 5Ni10La (c-d), and 5Ni10Nb (e-f) of reduced (a,c,e) and spent (b,d,f) catalysts.

Figure 2. TEM images of a) reduced NiLa b) reduced NiNb c) reduced Ni and d) spent Ni.

Figure 3. XPS Ni 2p of reduced 5Ni (A) and reduced 5Ni10Nb (B). XPS Nb 3d of reduced 5Ni10Nb (C). XPS Ni 2p and La 3d of reduced 5Ni10La.

Figure 4. Comparative H_2-TPR profiles of bare support, metal oxides, and Ni-free doped AC.

Figure 5. Deconvoluted H_2-TPR profiles of a) 5Ni, b) 5Ni10La, and c) 5Ni10Nb.

Figure 6. TPD-MS profiles for a) NH_3-TPD-MS (m/z = 15), b) CO-TPD-MS profiles (m/z = 28), c) CO-TPD-MS profiles (m/z = 44) for all catalyst samples.

Figure 7. Observed (colours) and alternative (grey) reaction network of HDO of HMF.

Figure 8. Temperature influence on product distribution over time using 5Ni/AC at a) 170 °C, b) 185 °C, c) 200 °C, d) 215 °C, e) 230 °C, and f) blank AC at 200 °C. ■ HMF, ● BHMF, ▼ 5-MF, ▲ 2-HM-5-MF, ★ DMF, ● BHMTHF, ◆ DMTHF, ▲ Humins. ---- Temperature. Model values correspond to lines, experimental values correspond with symbols.

Figure 9. Temperature influence on product distribution over time using 5Ni10La/AC at a) 170 °C, b) 185 °C, c) 200 °C, d) 215 °C, e) 230 °C, and f) 10La at 200 °C. ■ HMF, ● BHMF, ▼ 5-MF, ▲ 2-HM-5-MF, ★ DMF, ● BHMTHF, ◆ DMTHF, ▲ Humins. ---- Temperature. Model values correspond to lines, experimental values correspond with symbols.

Figure 10. Temperature influence on product distribution over time using 5Ni10Nb/AC at a) 170 °C, b) 185 °C, c) 200 °C, d) 215 °C, e) 230 °C, and f) 10Nb at 200 °C. ■ HMF, ● BHMF, ▼ 5-MF, ▲ 2-HM-5-MF, ★ DMF, ● BHMTHF, ◆ DMTHF, ▲ Humins. ---- Temperature. Model values correspond to lines, experimental values correspond with symbols.

Figure 11. Recyclability tests of Ni (left), NiNb (middle), and NiLa (right) catalysts. Dashed line represents when regeneration of the catalyst was performed.

Table 1. Textural properties of studied catalysts.

Sample	Ni loading (%)	Promoter loading (%)	S_{BET} ($m^2\ g^{-1}$)	t-plot micropore area ($m^2\ g^{-1}$)	t-plot external surface area ($m^2\ g^{-1}$)	t-plot pore volume ($cm^3\ g^{-1}$)	Avg. pore diameter (nm)
Bare AC	-	-	193	72	121	0.044	15.5
5Ni	5.4*	-	180	59	121	0.031	18.0
10La	-	-	73	3	70	0.001	27.6
5Ni10La	4.8*	10.3*	61	17	44	0.009	32.8
10Nb	-	-	203	70	133	0.041	15.1
5Ni10Nb	5.4*	8.3*	178	53	125	0.028	18.7

* Leaching of metallic species into the liquid phase following activity tests was determined to be negligible with <5 mg L^{-1} for Ni and <0.5 mg L^{-1} for La and Nb by ICP-OES analysis

Table 2. Quantitative results for total hydrogen consumption and for each deconvoluted peak.

Sample	T_{max} (°C)	H_2 Consumption [a] (mmol g^{-1})	H_2 Consumption below 400 °C (%)	Total H_2 Consumption (mmol g^{-1})
5Ni	218	0.008	41	0.230
	281	0.062		
	357	0.046		
	478	0.106		
	681	0.007		
5Ni10La	315	0.174	66	0.227
	450	0.064 [b]		
	797	0.053		
5Ni10Nb	312	0.057	41	0.153
	344	0.031		
	367	0.019		
	515	0.017		
	690	0.030		

[a] Experimental error for hydrogen consumption during H_2-TPR was determined to be ±5%.
[b] Excluding the peak representing LaO_2CO_3/ $LaOHCO_3$ identified in 10La/AC in Figure 3.

Table 3. Quantitative results for NH_3 and CO desorption and total concentration of sites.

Sample	Volume of NH_3 (mL)	Conc. Of Acid sites (μmol g^{-1})	Volume of CO (mL)	Conc. Of Metal Sites (μmol g^{-1})	Volume of CO_2 (mL)
5Ni	0.031	13	0.365	160	0.057
10La	0.193	86	0.330	144	0.206
10Nb	0.234	105	0.041	19	0.013
5Ni10La	0.043	19	1.03	489	0.267
5Ni10Nb	0.224	96	0.447	199	0.032

Experimental error for NH_3, CO, and CO_2 desorption was determined to be ±10%

Table 4. Calculated kinetic parameters and TOF for HMF hydrotreatment over Ni-based catalysts.

Reaction rate constants at 200 °C (k_i), min^{-1}				Activation energies (Ea_i), kJ mol^{-1}			Turnover Frequencies at 230 °C (TOF), min^{-1}		
i	5Ni	5Ni10La	5Ni10Nb	5Ni	5Ni10La	5Ni10Nb	5Ni	5Ni10La	5Ni10Nb
1	61±2	7.5±0.2	30.8±0.9	100±2	83±2	95±3	12.94	1.75	6.93
2	23.3±1.5	0.90±0.05	58±4	164±7	97±6	103±6	4.56	0.21	11.38
3	<0.1	<0.1	1.4±0.5	120±40	130±90	127±40	0.01	0.01	0.31
4	0.3±0.3	0.2±0.2	3.7±0.7	140±50	140±90	142±60	0.06	0.06	0.88
5	3.3±0.5	0.53±0.06	3.3±0.8	108±17	25±13	94±23	0.09	0.11	0.64
6	37±3	0.9±0.2	67±5	140±36	27±20	77±8	7.23	0.20	13.92
7	<0.1	<0.1	0.4±0.1[a]	n.a.	n.a.	>300	0	0	0.10
8	1.4±0.2	<0.1	3.8±0.3	210±22	n.a.	107±9	0.29	0	0.86

[a] Reaction rate constant given for 230 °C.